Energy Conversion and Management 251 (2022) 115009

Contents lists available at ScienceDirect

Energy Conversion and Management

journal homepage: www.elsevier.com/locate/enconman

Integrated optical-thermal-electrical modeling of compound parabolic concentrator based photovoltaic-thermal system

Anandhi Parthiban [a], T.K. Mallick [b], K.S. Reddy [a,*]

[a] Heat Transfer and Thermal Power Laboratory, Department of Mechanical Engineering, Indian Institute of Technology Madras, Chennai 600 036, India
[b] Environment and Sustainability Institute, University of Exeter, Penryn, UK

ARTICLE INFO

Keywords:
Concentrated PV/T
Non-uniform heat flux
Optical analysis
Glazed and unglazed CPC
Coupled numerical model
Nusselt number of CPC

ABSTRACT

The main aim of this work is to propose an integrated optical, thermal and electrical model to obtain the overall performance of a concentrated photovoltaic-thermal system (CPV/T). Monte Carlo ray-tracing (MCRT) simulations are done to obtain the flux profile on the absorber of a compound parabolic concentrator (CPC) for various angles of incidence. The obtained heat flux is mapped onto the solar cell in the finite volume method (FVM) to obtain its temperature profile. The modelling is done for both glazed and unglazed compound parabolic concentrator-photovoltaic/thermal (CPC-PV/T) systems using uniform (average heat flux) and non-uniform heat flux distribution. The obtained numerical results are compared with experimental results available in the literature. The results show that the prediction is accurate, with a maximum deviation in solar cell temperature of less than 3%. The deviations obtained when using non-uniform heat flux are much less than when using average heat flux. The temperature contours show that the temperature profile of the photovoltaic module obtained by using local non-uniform heat flux is different from the temperature profile obtained by using average heat flux, and these results will have a greater impact when designing a cooling system. The absorbed radiation from the optical analysis and average cell temperature from the thermal analysis are given to the five parameter electrical model of a solar photovoltaic cell to obtain the electrical power output. With the results of the integrated optical-thermal and electrical model, the overall useful power from both glazed and unglazed CPC-PV/T systems is calculated. The results show that the performance of the unglazed CPC-PV/T system is superior to the glazed CPC-PV/T system in terms of electrical and overall system output. This work demonstrates the need for a local heat flux profile and a coupled multi-physics model to accurately predict the performance of a concentrated photovoltaic/thermal (CPV/T) system.

1. Introduction

A solar photovoltaic (PV) cell absorbs the incident solar radiation and converts it into electricity. Harnessing solar energy using solar PV technology is highly attractive, but the semiconductor solar cells have an inherent drawback that they cannot completely utilize the entire spectrum of incident solar radiation, resulting in poor photovoltaic conversion efficiency. This implies that a major portion of the incident solar energy is dissipated as heat, causing the temperature of the PV cells to rise. Solar photovoltaic cells operating at high temperatures suffer from reduced electrical conversion efficiency, increased stress, and reduced panel life [1,2]. Hence, efforts are needed to maintain the operating temperature of the PV within the nominal value. The removal of waste heat from the PV panel offers low-temperature thermal output alongside reducing the panel temperature to which the electrical conversion efficiency is sensitive. Solar collectors that allow the simultaneous generation of both electrical and thermal energy are called hybrid solar photovoltaic/thermal (PV/T) collectors. The extraction of both electrical and thermal energy improves the system's reliability and overall efficiency [3]. The PV/T system is classified into two categories as thermally coupled and thermally decoupled PV/T systems depending on how the energy is delivered to the thermal absorber [4]. A thermally coupled PV/T system is analyzed in this work in which the entire spectrum of available solar energy is incident on the PV module.

Various active and passive methods of recovering the waste heat from the panel have been reported in the literature [5]. Some techniques also involve a combination of an active and passive cooling method to achieve thermal management of PV. Nasef et al. [6] proposed a two-dimensional numerical model for the concentrated photovoltaic-

* Corresponding author.
E-mail address: ksreddy@iitm.ac.in (K.S. Reddy).

https://doi.org/10.1016/j.enconman.2021.115009
Received 24 August 2021; Received in revised form 8 November 2021; Accepted 9 November 2021
Available online 27 November 2021

Nomenclature

A	area, m^2
a	diode ideality constant
CR	concentration ratio
C_p	specific heat, J kg^{-1} K^{-1}
C_1-C_6	correlation constants
E_g	band gap energy of semiconductor, eV
f	focal length of parabola, m
g	gravitational acceleration, m s^{-2}
H	height of CPC, m
h	heat transfer coefficient, W m^{-2} K^{-1}
I	current, A
I_o	reverse saturation current, A
I_{pv}	photovoltaic current, A
I_{sc}	short-circuit current, A
K	Boltzmann constant, J/K
K_I	temperature coefficient of $I_{sc,}$ %/°C
K_V	temperature coefficient of $V_{oc,}$ %/°C
L	length of the collector, m
m	refractive index
$\dot{m}$	mass flow rate, kg s^{-1}
N_s	number of cells connected in series
$\overline{Nu}$	average Nusselt number
P	pressure, Pa
$\dot{Q}$	volumetric heat generation, W m^{-3}
Q	heat flux, W m^{-2}
Q_u	useful energy, W
q	electron charge, C
R	correlation coefficient
R_p	shunt resistance, Ω
R_s	series resistance, Ω
S	concentrated radiation at the exit aperture of CPC, W m^{-2}
T	temperature, K
t	thickness, m
u	velocity, m s^{-1}
V	voltage, V
V_{in}	inlet velocity, m s^{-1}
V_{oc}	open circuit voltage, V
V_t	thermal voltage of module, V
V_w	wind velocity, m s^{-1}
W	width, m
x,y,z	Cartesian coordinate
x',y'	Cartesian coordinate of truncated parabola

Greek symbols

α	absorptivity
β	slope angle, degree
β_{cell}	temperature coefficient of the solar cell, /°C
γ	surface azimuth angle, degree
δ	declination angle, degree
ε	emissivity
η	efficiency, %
θ_A	half acceptance angle, degree
θ_i	incidence angle, degree
λ	thermal conductivity, W m^{-1} K^{-1}
μ	viscosity, kg m^{-1} s^{-1}
ρ	density, kg m^{-3}
σ	Stefan-Boltzmann constant, $= 5.67\times10^{-8}$ W m^{-2} K^{-4}
τ	transmissivity
ϕ	latitude, degree
ψ	transverse tilt, degree
ω	hour angle, degree

Subscripts

a	aperture
abs	absorber
amb	ambient
c	convective
cell	solar photovoltaic cell
Ew	existing work
ele	electrical
ext	external
f	fluid
g	glass cover
geom	geometric
gz	glazing
i	incident
in	inlet
n	nominal
opt	optical
out	outlet
PV	photovoltaic
Pw	present work
r	receiver/absorber
ra	radiative
ref	reference
t	truncation
td	tedlar
th	thermal
ti	thermal insulation
tot	total
u	useful

Abbreviations

CR	concentration ratio
DNI	direct normal irradiance
CPC	compound parabolic concentrator
CPVT	concentrate photovoltaic/thermal
ECPC	elongated compound parabolic concentrator
EMR	eliminating multiple reflections
LPM	liter per minute
MCRT	Monte Carlo ray-tracing
PCM	phase-change materials
PV	photovoltaic
PV/T	photovoltaic/thermal
STC	standard test condition
TEG	Thermo electric generator
UDM	user defined memory
UDS	user defined scalar
UDF	user defined function

thermal (CPV/T) system that is cooled by a combination of active and passive cooling methods. A closed-loop circulation of water is used to remove the heat from the PV panel, which is then transferred into the phase change material (PCM) panels placed inside the water tank. The proposed method of cooling showed a reduction in the average temperature of PV by 60%. Yazdanifard et al. [7] developed a detailed dynamic model to describe the performance of a concentrated PV/T system integrated with PCM-nano fluid. The results showed that combining PCM and nano-fluid improved the system's energy and exergy efficiency over a conventional concentrated PV/T system. The passive methods of cooling the solar panels are: fins [8,9], phase-change materials (PCM) [10,11], panel perforation [12], liquid immersion [13]

and radiative cooling [14]. The active methods of heat recovery are: forced circulation of heat transfer fluid such as air [15], water [16] and nano-fluid in water [17,18], thermoelectric generator (TEG) [19], jet impingement [20], water spraying [21], and heat pump [22].

PV panel cooling using water is accomplished either by placing ducts carrying water underneath the panel or by spraying water over the panel surface. Bahaidarah [23] experimentally investigated the efficacy of water jet impingement cooling in achieving temperature homogeneity to overcome hotspot generation and current mismatch in a concentrated PV system. The use of spray cooling results in high water and power consumption, but an efficient cooling system must offer high electrical conversion efficiency, better temperature homogeneity at minimum water, and pumping power requirements [24]. Cooling of PV panels with water is effective due to the better thermo-physical properties of water in comparison with air [25]. Gholami et al. [26] optimised a PV/T system by taking electrical, mechanical, and economic factors into account. The active ventilation employed to absorb the thermal power boosted not only the electrical efficiency but also the system's total efficiency by up to 85%. For techno-economic reasons, forced circulation of water inside the cooling tube is found to be the efficient way of removing the excess heat from the panel as it offers better temperature homogeneity with reduced pumping power consumption [27]. Though cooling offers an overall increase in the system efficiency, the electrical efficiency sees only a marginal increase [28]. The additional electrical power obtained using active cooling is lost in pumping the water through the cooling tubes; hence, it is not economical to invest in cooling for the flat PV system. However, the use of cooling along with a concentrator can make the PV system more economic.

Cooling of PV at a high mass flow rate efficiently improves the electrical efficiency, but the thermal gain is reduced drastically. This shows that the objectives of achieving high thermal and electrical gain from the PV/T system contradict design and operation parameters, and hence optimization of cooling system design for maximum electrical and thermal power output is required [29]. The PV/T systems can supply only low-temperature thermal output, which limits the use of extracted thermal energy. To extract thermal energy at medium and high temperatures, solar concentrators are essential. The concentration of solar radiation on the PV/T module not only increases the electrical power output but also increases the temperature at which the thermal energy is available. The concentrated PV/T system uses mirrors/reflectors to bring more radiation onto the solar cell, thereby increasing the power output from the system.

Solar concentrators have gained popularity in recent decades due to their ability to increase power output while lowering system cost [30,31]. Integration of the concentrator increases the incident power density, which increases the power output per unit area of solar cells. The barrier to adopting concentrators for solar PV applications is the non-uniform illumination, which produces hotspots that degrade the performance of the system. The non-uniformity in flux distribution is attributed to the continuous parabolic profile of the reflector [32]. Proper design of the cooling system and concentrator can eliminate the temperature hotspots to improve the reliability of the concentrated PV/T system. Some of the ill effects of non-uniform illumination on the electrical performance of PV cells are an increase in ohmic losses, decrease in voltage, current mismatch, decrease in electrical efficiency, and drop in fill factor (FF) [33]. The non-uniform temperature distribution associated with non-uniform illumination creates hotspots that may damage the solar cell over time. Baig et al. [34] have given a comprehensive review of various sources, effects, and mitigation methods of non-uniform illumination. Hence, it is very important to identify the regions of local hotspots to come up with a proper cooling system design. Different types of solar concentrators exist, but the compound parabolic concentrator (CPC) has been proven effective for solar PV panels due to its wide acceptance angle and maximum concentration efficiency [35]. CPCs having a concentration in the range 2× -10× do not need a continuous tracking system and constitute the low-concentration concentrators. From the design perspective, several modifications are applied to CPC to achieve flux uniformity and some of them are lens-walled CPC [36], segmented CPC [37], elimination-of-multiple-reflection (EMR) CPC [38], and elongated CPC [39]. Concentrating solar photovoltaic are restricted to low concentration levels as they cannot withstand very high temperatures associated with high concentration [40].

CPC used for the PV/T system can be glazed or unglazed depending on the grade of output energy required. It is recommended to go with an unglazed CPC-PV/T system for increased electrical gain and a glazed CPC-PV/T system for increased thermal gain [41]. Apart from the energy aspect, glazing protects the reflectors and solar cells against the accumulation of dust and moisture. Although the unglazed CPC system offers better electrical output, its performance deteriorates in the long run. Rahman et al. [42] discussed various parameters that affect the performance of PV panels, including dust cover and humidity. They observed that the electrical power decreases with an increase in humidity and dust accumulation. Aldihani et al. [43] found that the electrical power output decreased by 16% in the presence of a dust cover. Hence, the use of glazing is highly recommended in environments with high humidity and dust deposition. Various numerical and experimental studies on glazed CPC are available in the literature. The existing numerical studies have estimated the heat losses inside the glazed CPC to those occurring inside a comparable geometry such as a rectangular cavity, trapezoidal cavity, parallel plate, and V-trough, which may yield inaccurate results [44]. In the majority of the 1-D numerical analysis based on energy balance, the natural convection inside the CPC has been approximated to natural convection between horizontal parallel plates [45,46]. They neglected the effect of bounding walls and coupled convection-radiation effects.

Numerical simulations are an indispensable tool when testing the performance of the system for different design modifications. Several works exist on the numerical analysis of the concentrated PV/T system. Elsafi et al. [32] developed a thermal-electrical model to characterize the CPC-PV/T system. They used the five-parameter electrical model of solar cells to accurately determine the electrical parameters of the solar cell, which are then coupled to the thermal model. The simulation results showed that the CPC-PV/T systems have a greater output potential than the conventional flat hybrid PV/T systems. Sharaf and Orhan [47] developed a component-level thermodynamic model and simulation algorithm to evaluate the performance of the CPV/T system. Chandan et al. [48] studied the optical, thermal, and electrical performance of the ECPC-PV/T system using an analytical model. Al-Nimr and Dahdolan [49] developed a steady-state mathematical model based on energy balance to characterize the performance of concentrated PV/T that can supply electrical energy and distilled water. El-Samie et al. [50] conducted a numerical study on a concentrated PV/T system using a multiphysics model to investigate the performance of different heat sink designs. Li et al. [51] examined the performance of crystalline silicon solar cells combined with CPC for non-uniform and uniform flux distributions. The results demonstrated that the non-uniform distribution of flux on the solar cells improved the electrical output.

Lamba and Kaushik [52] developed an analytical model to simulate the performance of the concentrated PV-TEG hybrid system. It has been demonstrated that the concentrated PV/TEG system produces more power than a standard PV-only system. Soltani et al. [53] modeled a trigeneration system consisting of PV/TEG integrated with parabolic trough collector (PTC). A set of non-linear algebraic equations were arrived at and then solved using the iterative Newton-Raphson technique to obtain the electrical and thermal characteristics of the system. Shadmehri et al. [54] developed a comprehensive three-dimensional numerical model for the novel concentrating PV/T system with TEG integrated between the solar cell and the triangular cooling duct. The concentrator integrated into the system is a PTC whose optical characteristics are obtained using the Monte Carlo ray-tracing (MCRT) simulations and it is coupled to the finite volume method (FVM) to obtain the

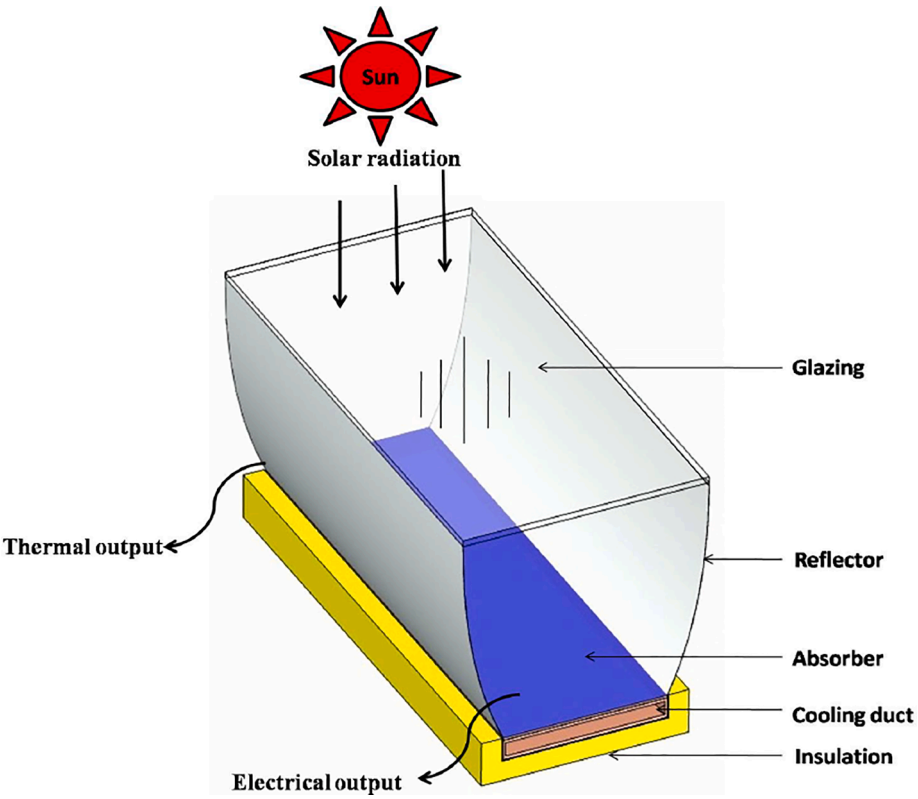

Fig. 1. Glazed CPC-PV/T system.

heat transfer and fluid flow characteristics. This method of modeling CPV/T systems using a combination of MCRT and FVM has been shown to provide reliable accuracy, which considerably aids in the design of CPV/T systems.

The existing analytical models are based on energy balance in which a set of non-linear partial differential equations are arrived at and then solved using iterative numerical techniques to obtain the temperatures [55,56]. These models are insufficient when crucial design attentions concerning thermal homogeneity are to be modeled. The earlier studies have assumed the solar flux distribution as uniform but in reality, the concentrated heat flux at the absorber is non-uniform, resulting in uneven heating of the absorber. To obtain the precise features of the system, a three-dimensional numerical model counting the nature of non-uniform heat flux is required. The non-homogeneous heat flux severely affects the electrical performance of the collector, but the state-of-the-art numerical studies have not considered the same while modeling the collector's performance [57,58]. Zhang et al. [33] pointed out that the use of average values in numerical simulations is insufficient to accurately obtain the actual temperature profile and electrical performance of the PV cell. To the best of the author's knowledge, no numerical study on concentrated PV/T system has hitherto considered non-uniform illumination and temperature while modeling the thermal-electrical performance of the CPC- PV/T collector. Existing works have studied the optical, thermal, and electrical performance of the concentrated photovoltaic/thermal (CPV/T) system separately, but a numerical study with an integrated optical, thermal, and electrical model to obtain the overall performance of the system is rarely found.

A three-dimensional, steady state integrated optical-thermal and electrical model is developed in this work to determine the overall system performance of the CPC-PV/T collector. The optical analysis is done for both glazed and unglazed CPC for various angles of incidence. The obtained non-uniform heat flux is mapped onto the solar cell to simulate the thermal performance. For the glazed CPC, the authors propose a correlation for the heat loss in a glazed CPC based on recent work [59]. Instead of approximating the heat loss to an equivalent geometry as found in existing works, we propose a correlation for the heat loss inside a glazed CPC. The thermal model uses cell temperature-dependent volumetric heat generation as a boundary condition to predict the temperature distribution in the collector, which further increases the accuracy of the suggested model [60]. The cell temperature and the absorbed incident radiation obtained from the thermal and optical models are coupled to the lumped-parameter electrical model to obtain the electrical power output from the system. In this work, the central aim is to improve the accuracy of modeling a CPC-PV/T collector by using a local heat flux profile in a coupled optical-thermal and electrical model so that design modification can be tested at greater accuracy.

2. System configuration and heat losses in a CPC-PV/T system

The concentrated PV/T system has optical elements called concentrator attached to the PV/T collector. The solar rays, after reflection from the reflectors, arrive at the photovoltaic module installed at the CPC's exit aperture. The solar photovoltaic module converts incident solar energy into electrical energy, while the heat generated in PV is recovered by the solar thermal collector mounted at the bottom of the photovoltaic module. Water is forced via a cooling duct attached to the bottom of the solar cells to recover the excess heat. The various losses during the conversion of incident light into electrical and thermal energy in a CPV/T collector are optical, thermal and electrical losses.

2.1. System description

The system consists of a PV/T collector with CPC integrated on top of it. Both in the glazed CPC and the unglazed CPC systems, the solar cell is sandwiched between the layer of glass cover and Tedlar. The PV module analysed in this work is a commercial module in which the solar cell is properly sealed between the glass cover and Tedlar to prevent dust and

moisture from entering the cell. Fig. 1 shows the glazed CPC based concentrated PV/T system. A rectangular aluminium channel of dimension 130 mm × 1016 mm × 13 mm is attached to the bottom surface of the Tedlar for removing the excess heat from the solar cells. The solar PV cells along with the cooling duct are insulated at the sides and bottom and are kept inside an aluminium casing. Thermal insulation at the sides and bottom prevents any heat loss to the environment. The dimensions along with the thermo-physical properties of various layers that make up the PV/T system are given in Table 1. The unglazed CPC allows for enhanced heat loss from the collector due to external wind directly removing the heat from the absorber, thereby lowering the panel temperature that aids in increased electrical conversion efficiency. In a glazed CPC-PV/T system, the glazing traps solar radiation that increases the collector temperature, which can be removed by water, thereby increasing the temperature of the thermal output.

2.2. Heat losses in a CPC-PV/T system

In this section, the various pathways through which the concentrated PV/T system loses heat to the environment are explained in detail. The optical and thermal losses in a glazed and unglazed CPC-PV/T system are given in Fig. 2. When solar radiation strikes the CPC glazing, a small portion of it is absorbed by the glazing before being transmitted in to the CPC. Inside the CPC, the rays undergo multiple internal reflections before arriving at the PV. The concentrated rays arriving at the PV generate electrical and thermal energy. The photoelectric conversion efficiency of solar cells is temperature-dependent and it increases with a decrease in cell temperature. The photoelectric conversion efficiency of solar cells is given by Evans [61] as in Eq. (1),

$$\textit{Photo} - \textit{electric conversion efficiency of solar cell},\quad \eta_{cell} = \eta_{ref}\left[1 - \beta_{cell}\left(T_{cell} - T_{ref}\right)\right] \tag{1}$$

where η_{ref} is reference efficiency of the solar cell and is taken as 15% at a reference temperature (T_{ref}) of 25 °C, and β_{cell} is the temperature coefficient of the solar cell and is taken as 0.0045/°C for silicon solar cells [61]. The heat from the bottom surface of the solar cell reaches the cooling duct after conduction through Tedlar. The outer surface of the cooling duct loses heat to the ambient after conduction through insulation. The heat from the inside of the cooling duct is recovered by water running through the duct. The convection inside the cooling duct can be laminar or turbulent, depending on the flow rate.

The heat generated by the solar cell is transferred to the top glass of the solar cell via conduction. From the top of the PV glass the heat is further lost to the ambient by convection and radiation. In the case of an unglazed CPC system, the heat from the PV glass cover is directly lost to the surrounding by convection and radiation. The convection is due to external wind flowing over the collector surface and the radiation is due to radiative exchange between PV glass cover and sky. The convection and radiation heat loss from the PV glass cover to the atmosphere in an unglazed system are given by Eqs. (2) and (3) [62]. The wind convection coefficient and radiation heat loss coefficient are given in Eqs. (4) and (5) [63].

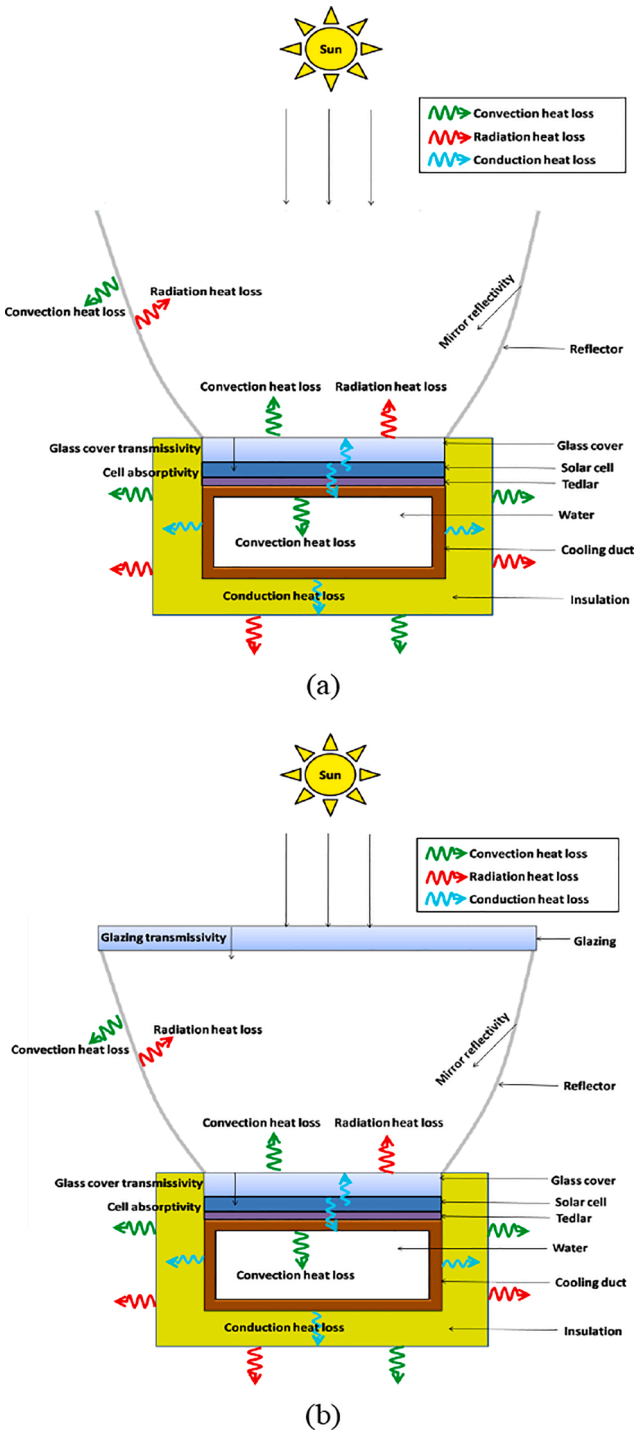

Fig. 2. Optical and thermal losses in a CPC-PV/T system: (a) Unglazed and (b) Glazed.

Table 1
Thermo-physical properties of various layers of PV/T collector [60].

Layer	Thickness (mm)	Thermal conductivity (W/m-K)	Density (kg/m^3)	Specific heat capacity (J/kg-K)
Glazing	1.5	1	3000	500
Glass cover	1.5	1	3000	500
PV	0.3	148	2330	677
Tedlar	0.3	0.15	1200	1250
Cooling channel (Aluminium)	1	204	2710	910
Water	–	0.63	998.2	4183

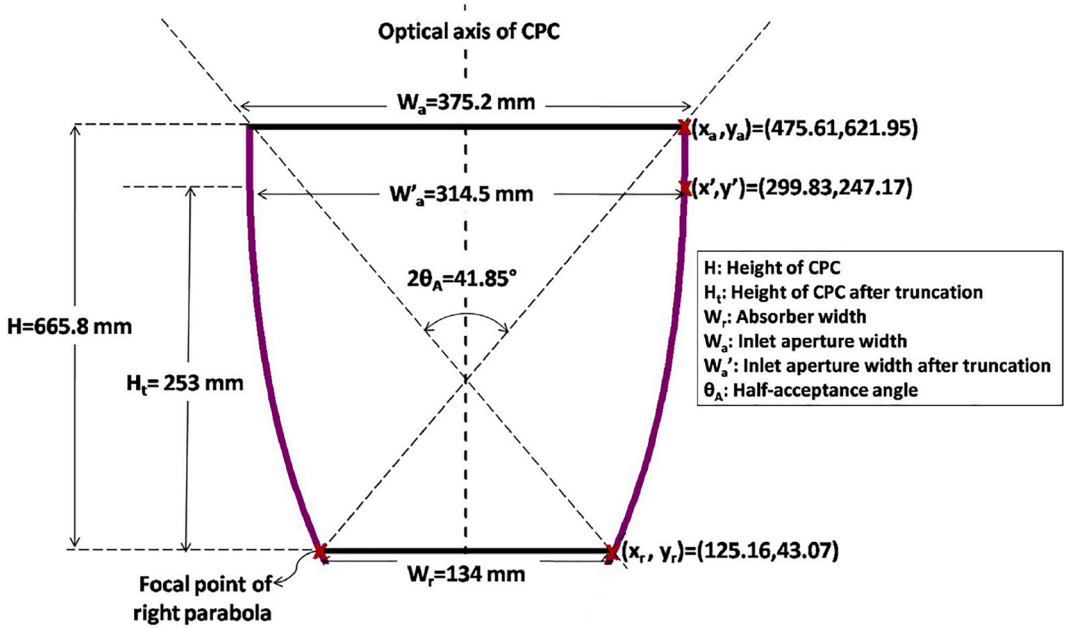

Fig. 3. Geometry of 2-D compound parabolic concentrator.

$$\textit{Convection heat loss from PV glass cover to ambient, } Q_{c,g-amb} = h_{c,g-amb}\left(T_g - T_{amb}\right) \tag{2}$$

$$\textit{Radiation heat loss from PV glass cover to the sky, } Q_{ra,g-sky} = h_{ra,g-sky}\left(T_g - T_{sky}\right) \tag{3}$$

$$\textit{Wind convection coefficient, } h_{c,g-amb} = 5.7 + 3.8V_w \tag{4}$$

$$\textit{Radiation heat loss coefficient, } h_{ra,g-sky} = \sigma\varepsilon_g\left(T_g^2 + T_{sky}^2\right)\left(T_g + T_{sky}\right) \tag{5}$$

Where $h_{c,g-amb}$ is the convective heat loss coefficient from glass cover to ambient, $h_{ra,g-sky}$ is the radiative heat loss coefficient from glass cover to sky, V_w is external wind velocity and $\varepsilon_g$is the emissivity of glass cover. In the case of a glazed CPC-PV/T system, the heat from the PV glass reaches the glazing via natural convection and radiation before dissipating into the ambient. The heat loss inside the CPC is due to natural convection caused by differential heating of air between the hot PV glass and cold glazing. The top heat loss coefficient for the glazed CPC-PV/T system is computed using the correlation proposed by the authors based on the previous work [59].

3. Integrated optical-thermal-electrical model

To accurately predict the performance of the CPC-PV/T collector, a fully coupled multi-physics model is proposed. The multi-physics integrated model comprises an optical model for computing the heat flux, a thermal model for computing the cell temperature, and an electrical model for computing the electrical power output, all of which are precisely coupled together. To obtain the thermal characteristics of the system, the non-uniform heat flux obtained from 3D ray tracing is mapped on to the solar cell in the finite volume method. The thermal boundary condition is the volumetric heat generation in solar cells that corresponds to non-uniform heat flux. The absorbed heat flux from the optical model and the cell temperature from the thermal model are imparted to the electrical model to obtain the electrical power produced by the system. For the heat loss in a glazed CPC, a correlation is proposed for the average total Nusselt number as a function of absorber temperature, ambient temperature, absorber emissivity, external heat loss coefficient, truncation and angular orientation.

3.1. Optical model

Monte Carlo ray-tracing simulations are done to obtain the incidence angle dependent flux distribution profile. The performance of both glazed and unglazed CPC is studied for various angles of incidence.

3.1.1. Design of CPC

The geometry of CPC as shown in Fig. 3 consists of two parabolic segments crossed in such a way that the focal point of one parabola lies exactly on the other. The angle between the optical axis of CPC and the line connecting the focal point of a parabola with the edge of the parabola at the inlet aperture is called the half acceptance angle. Any ray that is incident on the inlet aperture at an angle less than or equal to the acceptance angle makes its way to the absorber located at the exit aperture through multiple internal reflections. The CPC is a static 2D concentrator whose geometric concentration ratio is given in Eq. (6).

$$\textit{Geometric concentration ratio, } CR_{geom} = \frac{m}{sin\theta_A} \tag{6}$$

where m is the refractive index of the medium and is 1 for air-filled CPC and θ_A is the half acceptance angle.

The effective concentration ratio taking reflection losses into account is called optical concentration ratio and it depends on the incidence angle, reflector shape and material [64]. The optical concentration ratio is given as Eq. (7)

$$\textit{Optical concentration ratio, } CR_{opt} = CR_{geom}\eta_{opt} \tag{7}$$

Where $\eta_{opt}$is optical efficiency of CPC and is defined as the ratio of solar energy available at the exit aperture of CPC to the solar energy incident at the inlet aperture of CPC and is given by Eq. (8).

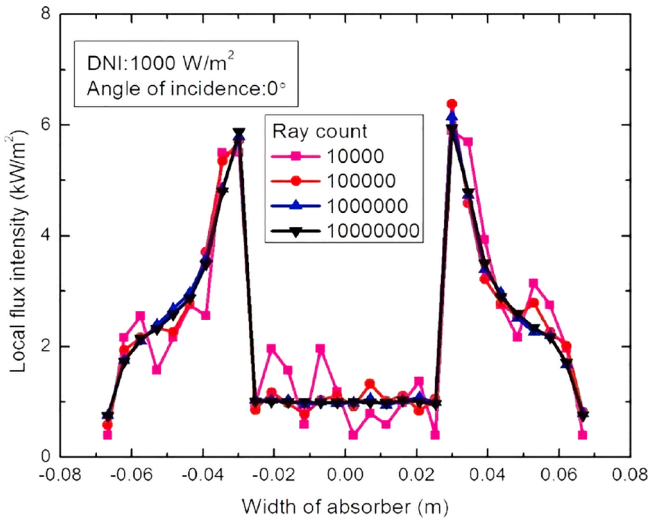

Fig. 4. Effect of number of rays generated: Variation of local flux intensity along the width of absorber.

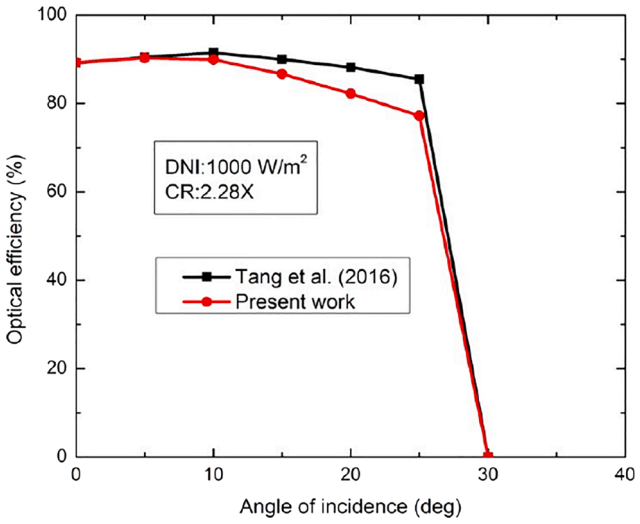

Fig. 6. Comparison of optical efficiency of unglazed CPC with that of work done by Tang et al. [68] with mirror reflectivity 85%.

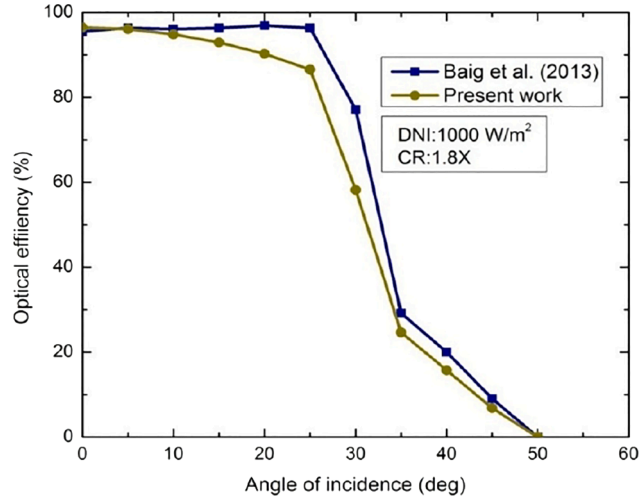

Fig. 5. Comparison of optical efficiency of unglazed CPC with that of work done by Baig et al. [67] with mirror reflectivity 92%.

$$Optical\ efficiency\ of\ CPC, \eta_{opt} = \frac{SA_r}{QA_a} \tag{8}$$

Where the inlet aperture (A_a) is the aperture of the CPC through which the incident solar rays enter the CPC, and the exit aperture (A_r) is the CPC aperture where the absorber is mounted. The term S in the above equation refers to the concentrated radiation at the CPC's exit aperture and the term Q refers to incident radiation at the inlet aperture of CPC. A CPC of 2.3× concentration having absorber width 134 mm is taken for the optical analysis. The equations for arriving at the geometry of the CPC are given by Eqs. (9)-(18) [35]. A basic parabola is generated in the x-y coordinate system and then it is rotated by half acceptance angle in a clockwise and anticlockwise direction to obtain the right and left parabola.

The equation of the parabola in x-y co-ordinate system is

Table 2
Optical properties of various layers of PV/T collector [60].

Layer	Transmissivity	Absorptivity	Reflectivity	Emissivity
Glazing	0.95	0.03	0.02	0.93
Glass cover	0.95	0.03	0.02	0.93
PV cell	–	0.88	0.12	–
CPC Reflector	–	0.05	0.92	–

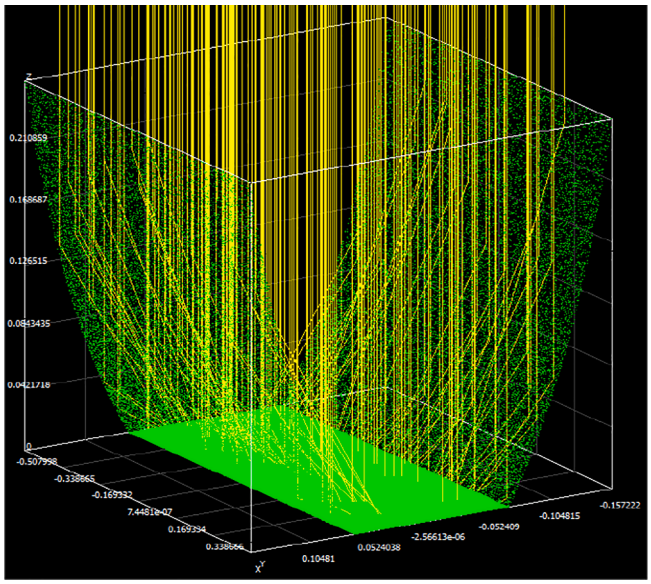

Fig. 7. Optical ray tracing of unglazed CPC.

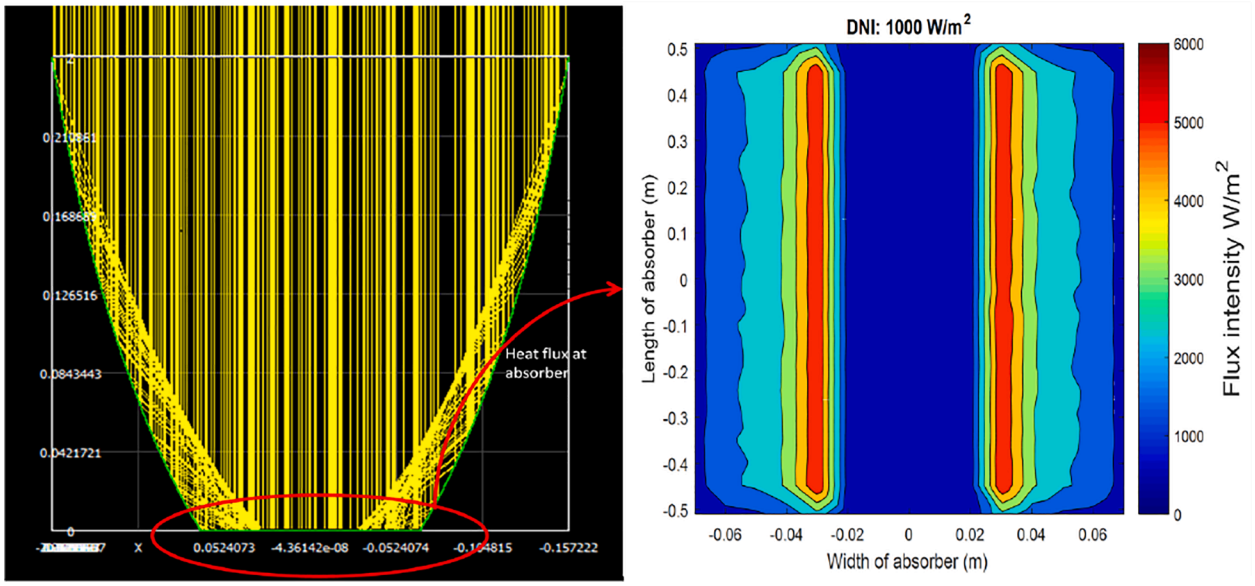

Fig. 8. Ray-tracing and heat flux map for the absorber.

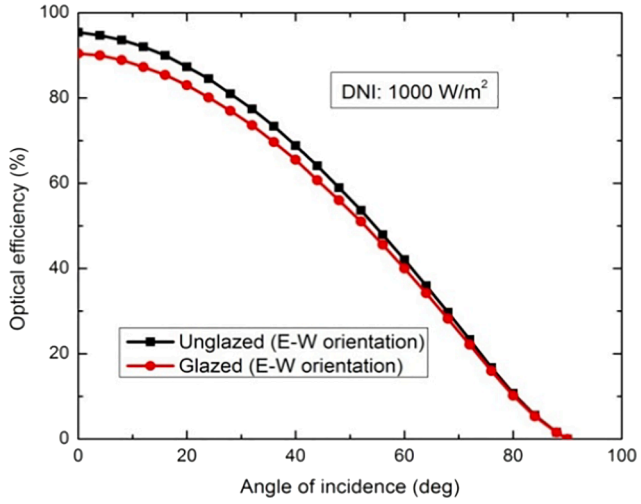

Fig. 9. Variation of optical efficiency of glazed and unglazed CPC in E-W orientation.

$$y = \frac{x^2}{2W_r(1+sin\theta)} \tag{9}$$

The focal length of parabola is given by

$$f = \frac{W_r}{2}(1+sin\theta) \tag{10}$$

The co-ordinates for the end points of the right parabola are

$$x_r = W_r cos\theta \tag{11}$$

$$y_r = \frac{W_r}{2}(1-sin\theta) \tag{12}$$

$$x_a = (W_r + W_a)cos\theta \tag{13}$$

$$y_a = \frac{W_r}{2}(1-sin\theta)\left(1+\frac{1}{sin\theta}\right)^2 \tag{14}$$

$$Height\ of\ CPC, H = \frac{W_r}{2}\left(1+\frac{1}{sin\theta}\right)cot\theta \tag{15}$$

The end point co-ordinate of truncated parabola is

$$x' = \frac{W_r}{2}\left[\frac{(1+\sin\theta)}{\cos\theta}\right]\left[-\sin\theta + \left(1+\frac{H_t}{H}cot^2\theta\right)^{1/2}\right] \tag{16}$$

The width at the inlet aperture after truncation is

$$W'_a = 2x'cos\theta - \frac{x'^2}{W_r(1+sin\theta)}sin\theta + W_r\left(sin\theta - cos^2\theta\right) \tag{17}$$

Height of truncated CPC

$$H_t = x'sin\theta + \frac{x'^2 cos\theta}{2W_r(1+sin\theta)} - \frac{W_r}{2}cos\theta(1+sin\theta) \tag{18}$$

3.1.2. Determination of angle of incidence

The CPC-PV/T collector is generally kept stationary with the horizontal axis of CPC along the E-W direction. The angle at which the solar radiation impinges on the inlet aperture of the CPC varies throughout the day due to the angular movement of the sun across the sky. This angular motion of the sun results in a variation in the optical efficiency of the CPC throughout the day. For the optical modeling of CPC, it is necessary to know the angle at which the solar rays impinge at the inlet aperture of CPC. The angle of incidence (θ_i) of beam radiation on the inlet aperture of CPC tilted about the horizontal plane can be expressed as a function of latitude (φ), hour angle (ω), surface azimuth angle (γ), collector slope (β), and declination angle (δ) [65]. The angle of incidence of beam radiation on a surface tilted about the horizontal plane is given by Eq. (19)

$$cos\theta_i = sin\delta\ sin\varphi\ cos\beta - sin\delta\ cos\varphi\ sin\beta\ cos\gamma + cos\delta\ cos\varphi\ cos\beta\ cos\omega + cos\delta\ sin\varphi\ sin\beta\ \cos\gamma\ \cos\omega + \cos\delta\ \sin\beta\ \sin\gamma\ \sin\omega \tag{19}$$

3.1.3. Optical modeling methodology and ray sensitivity study

The optical analysis of CPC is done using the optical modeling software SolTrace [66]. In SolTrace, the optical geometry is composed of stages in the global coordinate system. The stage consists of elements defined in the stage coordinate system. The first step in optical modeling is the location of the sun's position in the global coordinate system. The sun's position is defined in the form of a vector and is placed above the optical element. The optical property set is defined and this is later linked to various optical elements. The elements are generated; its surface, aperture, optical property set, and optical interaction are defined.

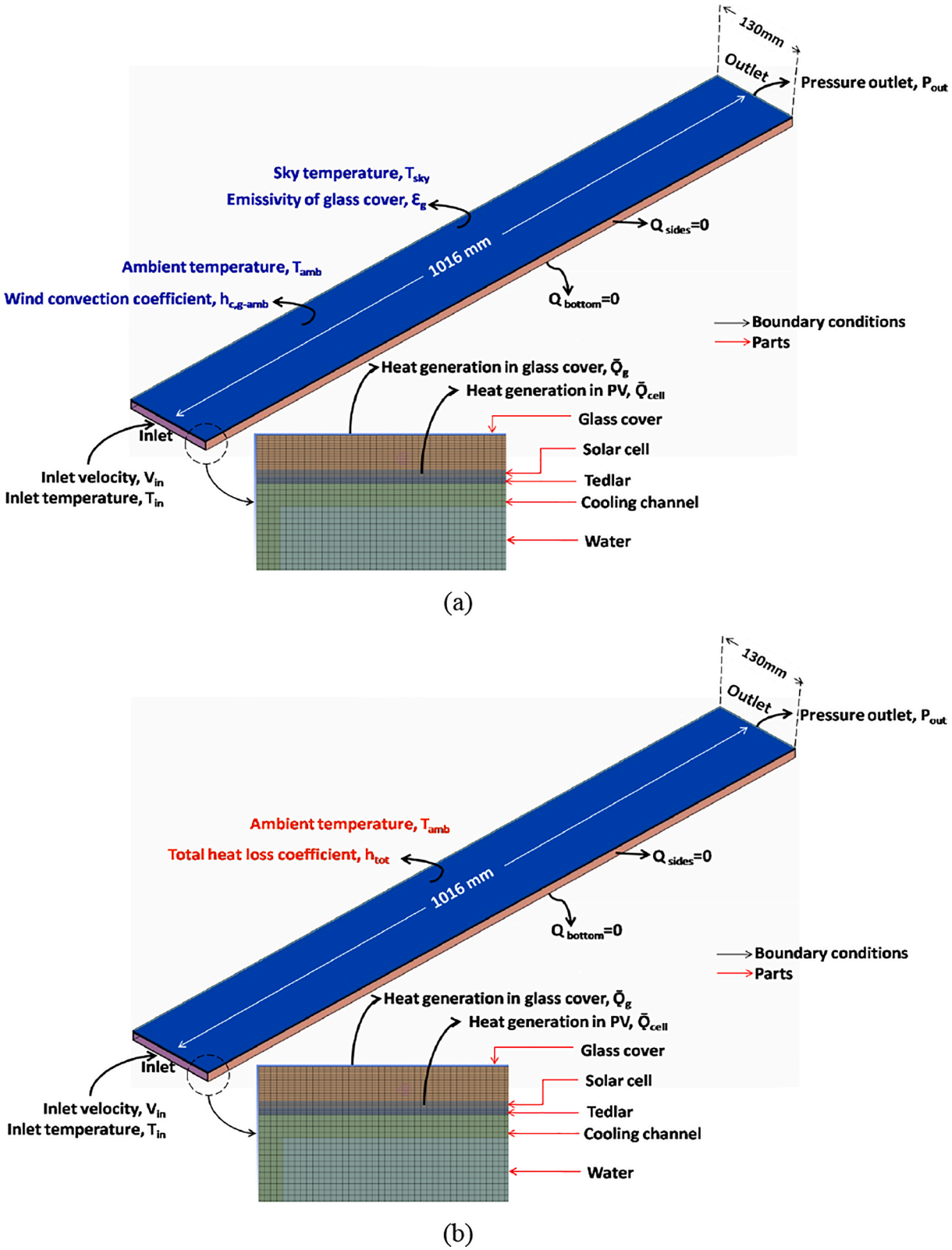

Fig. 10. Computational domain along with boundary conditions: (a) Unglazed CPC-PV/T system and (b) glazed CPC-PV/T system.

Once the sun's position, optical property, and elements are defined, the user sets the required DNI and the required number of rays to be traced through the geometry. The choice of the number of rays is based on the accuracy in results but at the cost of increased computational time.

The concentration ratio of the CPC modeled here is 2.3 × , obtained by truncation of 2.8× CPC having an absorber width of 134 mm. The 3-D geometry is created by extruding the CPC to a length of 1016 mm. Here the performance of both glazed and unglazed CPC is analyzed. The equations for generating the CPC and the coordinates of its endpoints are given in Eqs. (9)-(18). The CPC reflectors are made of highly reflective

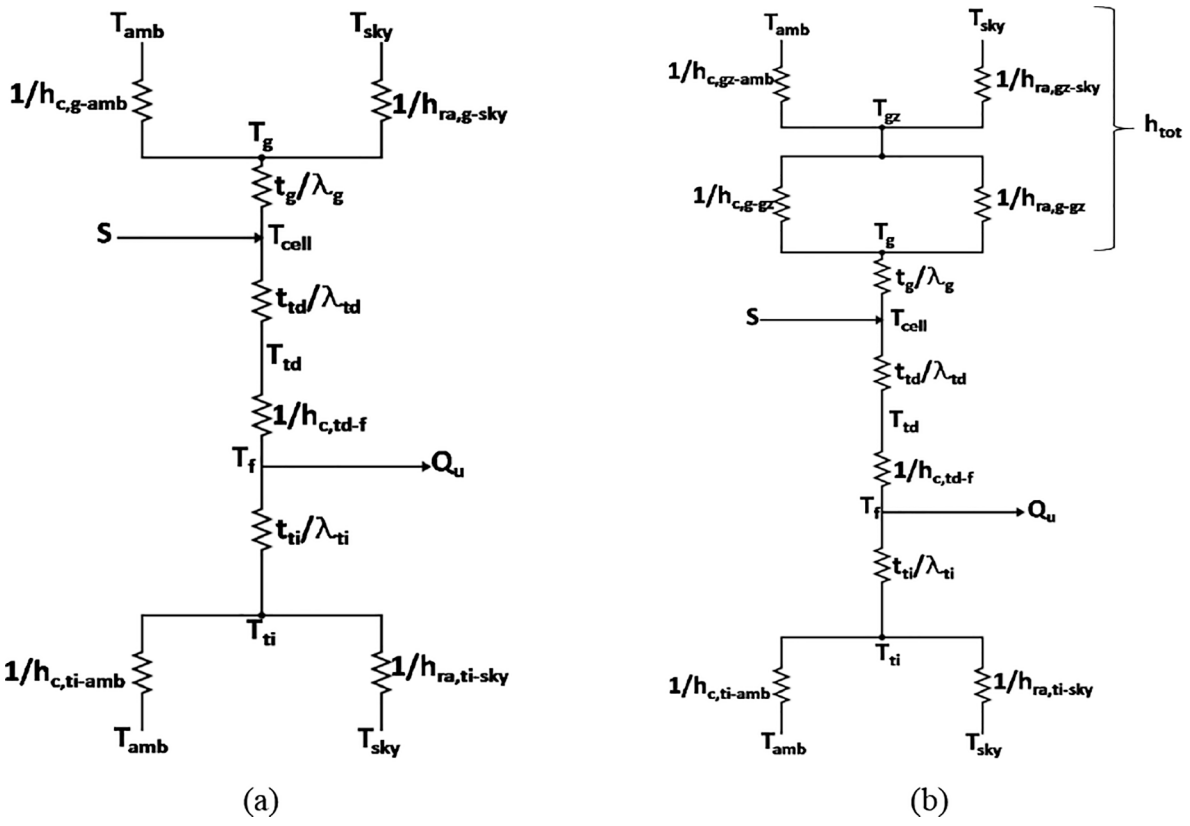

Fig. 11. Thermal resistance network: (a) Unglazed CPC-PV/T system and (b) glazed CPC-PV/T system.

mirrors with a reflectivity of 92%. The transmissivity of the glazing used in the glazed CPC system is 95%. Before proceeding with the actual optical analysis, the required number of rays to produce accurate results is obtained by performing a ray sensitivity study. The local flux distribution along the width of absorber for a different number of ray interactions at a zero-degree angle of incidence is shown in Fig. 4. From the figure, it can be seen that the local flux distribution stabilizes with the increase in the number of ray interactions. Based on this result, the number of ray interactions selected for our optical analysis is one million.

3.1.4. Validation

The optical analysis of CPC is validated against the numerical work done by Baig et al. [67] in which they have modeled the performance of 1.8× CPC (truncated from 2× CPC) under direct and diffused incident radiation. They analyzed the performance of both glazed and unglazed CPC and presented their optical efficiency as a function of incidence angle. The details of the CPC construction and its optical properties can be found in [67]. The optical efficiency obtained from the present work and that obtained by Baig et al. [67] is given in Fig. 5. Since the CPC is symmetric about its optical axis, the optical performance is shown for angular variation in only one direction. The maximum optical efficiency attained using present work is 96.45% and is obtained at zero-degree incidences. The deviation in optical efficiency is calculated using Eq. (20) where $\eta_{opt,Pw}$is the optical efficiency obtained using present work and $\eta_{opt,Ew}$is the optical efficiency obtained using existing work. The deviation in optical efficiency between the present work and that by Baig et al [67] is found to be 0.3%-25%.

$$\textit{Percentage deviation in optical efficiency} = \left|\frac{\eta_{opt,Pw} - \eta_{opt,Ew}}{\eta_{opt,Ew}}\right| \times 100 \qquad (20)$$

A second validation is provided for the optical analysis of CPC using the results reported in [68]. A full CPC of concentration ratio 2.28× is modeled in SolTrace for different angles of incidence and the resultant optical efficiency is reported in Fig. 6. The CPC modeled is a full CPC having a half-acceptance angle of 26°. The reflectivity of the CPC is taken as 85%. A deviation of 0.1%-9.6% is observed between the present work and the work reported in [68].

3.1.5. Optical efficiency of glazed and unglazed CPC

The optical analysis is performed for both glazed and unglazed CPC in E-W orientation and their resultant optical efficiencies are presented for angular variation in a day. The angular performance study is done by varying the angle of incidence of the rays on the inlet aperture of the CPC. The x, y, and z coordinates of the sun's position in the global coordinate system are varied to obtain the required angle of incidence. The optical properties of the glazing and reflectors are given in Table 2. The slope error and specularity error of the reflector are taken as a Gaussian distribution with an error value of 2 mrad [69]. The ray-tracing diagram of CPC is given in Fig. 7, in which only the first 200 rays are shown for the purpose of better visualization of ray interaction. The ray tracing along with the absorber flux map at normal incidence is given in Fig. 8. It can be seen that the flux distribution between −0.025 m and 0.025 m is uniform and is equal to 1000 W/m^2. This is because the region between −0.025 m and 0.025 m on the absorber receive light rays that are not intercepted by the reflectors. The incident rays that interact with the reflectors cloud near the edge of the absorber, and so the region near the edge of the absorber on both sides has maximum flux intensity. The location of maximum heat flux occurs at −0.03 m and + 0.03 m (width of absorber). The resultant optical efficiency of glazed and unglazed CPC for angular variation in incident light is given in Fig. 9. It can be seen that the optical efficiency of glazed CPC is less than that of the optical efficiency of unglazed CPC due to attenuation of incident light at the glazing. Also, the CPC in E-W orientation collects more energy in a day than the CPC oriented in the N-S direction (given in the Appendix).

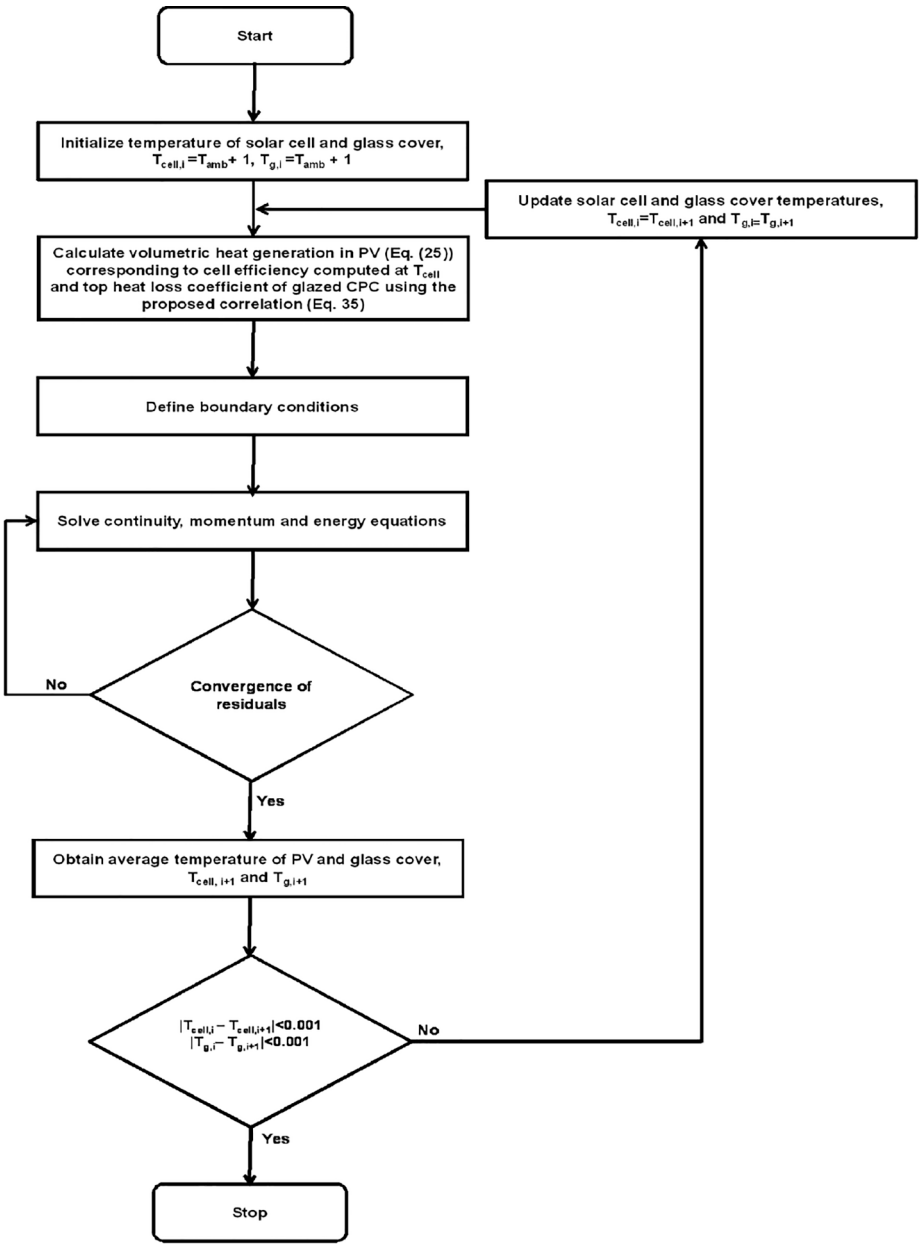

Fig. 12. Numerical procedure for thermal modeling of glazed CPC-PV/T system.

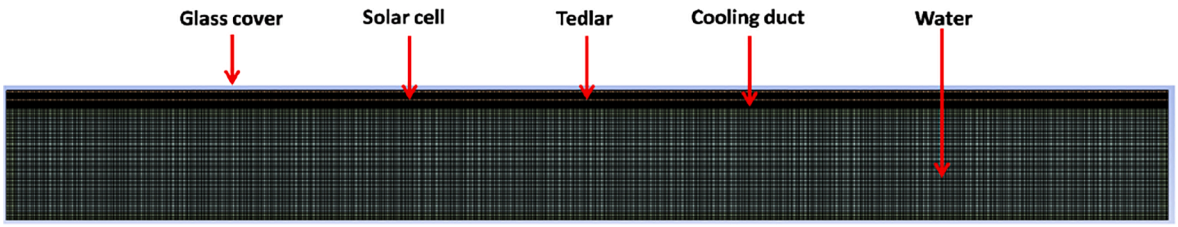

Fig. 13. Cross sectional view of meshing in computational domain.

3.2. Thermal model

A steady-state, three-dimensional thermal modeling of the solar CPC-PV/T collector is done using the ANSYS Fluent 2020 R1 finite volume solver. The thermal performance of both the glazed and unglazed CPC-PV/T system is modeled for the input conditions taken from the literature [41]. The performance of the CPC-PV/T system is studied under both uniform and non-uniform heat flux to obtain the average temperature of PV and outlet water temperature. The side and bottom losses are minimal and hence are neglected in the system modeled here.

3.2.1. Computational domain

The modeling is done using a three-dimensional computational domain of PV/T collector. The use of concentrated heat flux and CPC

Table 3
Variation of cell temperature with a change in element size.

Element size (m)	Number of elements	T_{cell} (K)	$\left\|\frac{T^{j}_{cell} - T^{j+1}_{cell}}{T^{j}_{cell}}\right\| \times 100$
1.00×10^{-3}	5,283,200	303.72	0.34
7.00×10^{-4}	12,704,956	302.69	0.28
5.00×10^{-4}	28,000,960	301.83	0.03
4.50×10^{-4}	37,245,710	301.73	0.03
4.00×10^{-4}	50,431,700	301.65	–

Table 4
Electrical characteristic of C60 mono-crystalline solar cell at STC [41].

Electrical parameter	Value
Maximum/Rated power (P_{mp})	3.40 W
Voltage at maximum power (V_{mp})	0.575 V
Current at maximum power (I_{mp})	5.92 A
Short circuit current (I_{sc})	6.28 A
Open circuit voltage (V_{oc})	0.680 V
Temperature coefficient of V_{oc} (K_V)	−0.2647 %/°C
Temperature coefficient of I_{sc} (K_I)	0.0414 %/°C

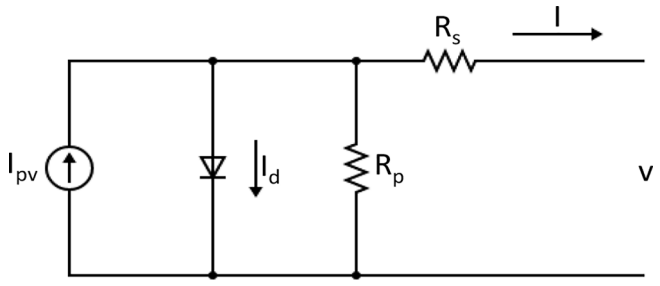

Fig. 14. Single diode equivalent circuit of solar PV cell.

heat loss coefficient from external sources helps to eliminate the CPC from the computational domain thereby reducing the computational overhead. The computational domain along with boundary conditions and meshing is given in Fig. 10. The assumption of adiabatic sides and bottom eliminates the need to model the system with insulation. The thermal resistive network of the modeled unglazed and glazed CPC-PV/T system is given in Fig. 11.

3.2.2. Governing equations and numerical procedure

The fluid flow and heat transfer are solved by solving for coupled continuity, momentum, and energy equations. For the solid domains, it is sufficient to solve energy equations, whereas for the fluid domain, it is required to solve continuity, momentum, and energy equations simultaneously. The flow rate considered in this study is 1 LPM. The Reynolds number calculated for the flow rate of 1 LPM is well within the critical range and hence the PV/T system is modeled for laminar flow. The turbulent natural convection and surface radiation inside the CPC cavity are modeled separately and the obtained heat loss coefficient is fed here, so there is no need to enable explicit models for modeling turbulent convection and surface radiation. The thermo-physical characteristics of the PV/T collector layers are assumed to remain constant with temperature change. From the law of conservation of mass, momentum, and energy, the transport equations for steady-state and single-phase fluid flow are Eqs. (21)-(23).

$$\textit{Continuity equation}, \frac{\partial}{\partial x_j}\left(\rho u_j\right) = 0 \tag{21}$$

$$\textit{Momentum equation}, \quad \frac{\partial}{\partial x_j}\left(\rho u_i u_j\right) = -\frac{\partial P}{\partial x_i} + \frac{\partial}{\partial x_j}\left[\mu\left(\frac{\partial u_i}{\partial x_j} + \frac{\partial u_j}{\partial x_i}\right)\right] + \rho g_i \tag{22}$$

$$\textit{Energy equation}, \frac{\partial}{\partial x_j}\left(\rho u_j C_p T\right) = \frac{\partial}{\partial x_j}\left[\lambda \frac{\partial T}{\partial x_j}\right] + \dot{Q} \tag{23}$$

The term $\dot{Q}$in the energy equation represents internal volumetric heat generation and is computed for the glass cover and solar cell using Eqs. (24) and (25). The solar cell is assumed to have zero transmissivity, and hence the layers that follow it will generate no internal heat. The heat generation in the PV glass cover is due to the absorption of solar radiation by the glass cover. The heat generation in a solar cell is due to unutilized absorbed energy after electrical energy conversion (solar heat load). The optical properties of the glass cover, PV, and reflector are given in Table 2. The numerical procedure adopted in solving the transport equations to obtain the temperature profile is depicted using a flow chart given in Fig. 12. As seen, an iterative process is used to obtain the actual solar cell heat generation and glass cover heat loss coefficient.

Table 5
Performance of unglazed CPC on experimental day (E-W orientation).

Time (h)	Angle of incidence (deg)	Incident radiation (W/m^2)	Average flux at absorber (W/m^2)	Peak flux at absorber (W/m^2)	Minimum flux at absorber (W/m^2)	Optical efficiency (%)	Actual CR
9	41.69	449	704	1840	311	66.84	1.54
10	27.34	587	1125	2839	488	81.74	1.88
11	12.97	767	1644	4035	684	91.35	2.10
12	−1.81	864	1928	4678	817	95.05	2.19
13	−15.97	691	1456	3608	616	89.78	2.06

Table 6
Performance of glazed CPC on experimental day (E-W orientation).

Time (h)	Angle of incidence (deg)	Incident radiation (W/m^2)	Average flux at absorber (W/m^2)	Peak flux at absorber (W/m^2)	Minimum flux at absorber (W/m^2)	Optical efficiency (%)	Actual CR
9	41.69	449	677	1793	298	64.20	1.50
10	27.34	587	1076	2727	456	78.14	1.83
11	12.97	767	1568	3865	646	87.14	2.04
12	−1.81	864	1834	4445	765	90.43	2.12
13	−15.97	691	1389	3462	570	85.68	2.00

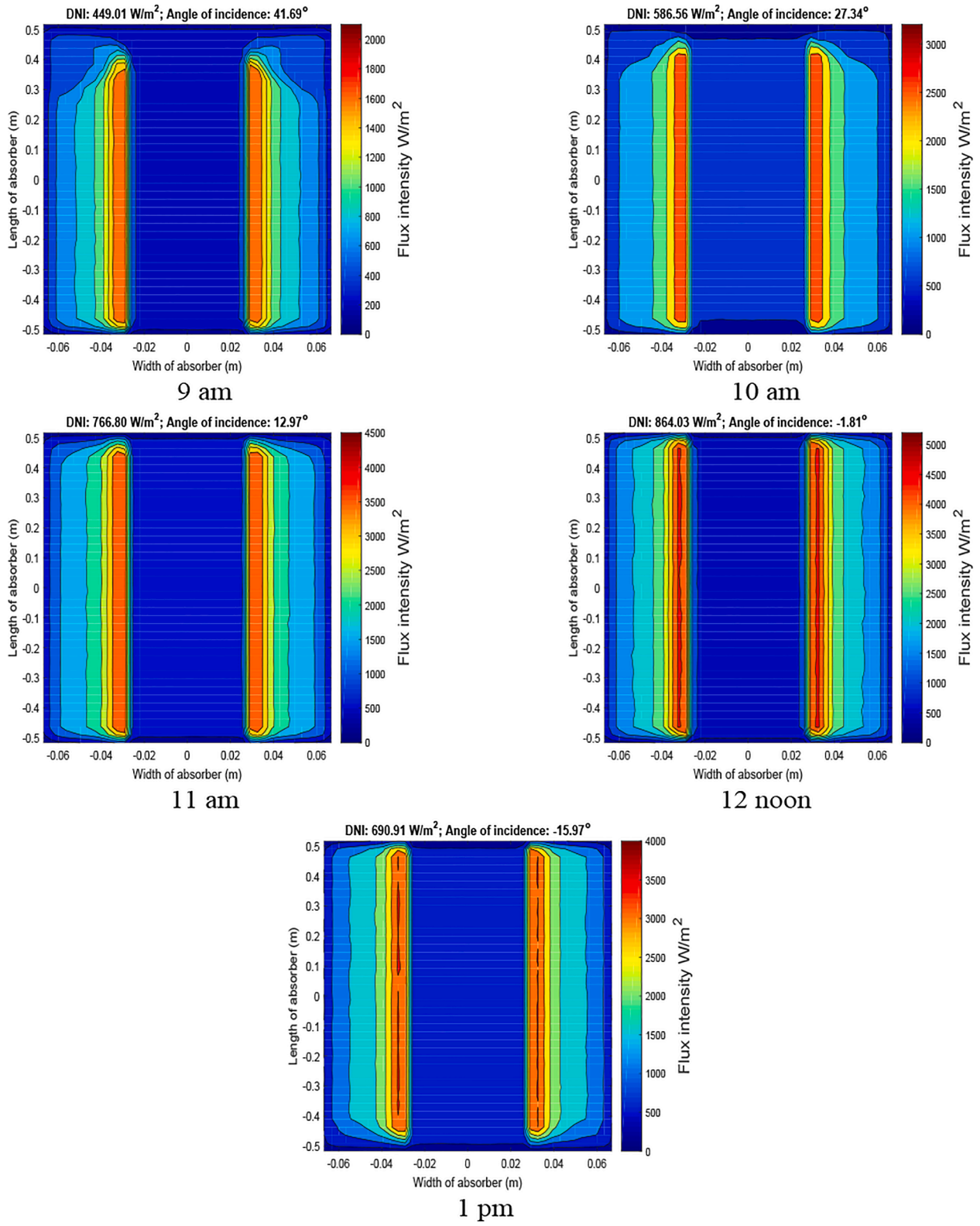

Fig. 15. Flux distribution on the absorber of unglazed CPC between 9 am and 1 pm.

The initial iteration is performed by assuming the temperature of the glass cover and the solar cell is one degree Celsius more than the ambient temperature. This is a good assumption for the initial iteration as the solar cell temperature is always expected to be higher than the ambient temperature when energy is incident on them. With this initial assumption, the heat generation in the solar cell and glass cover is calculated using Eqs. (24) and (25).

$$\textit{Heat generation in glass cover},\ \dot{Q}_g = \frac{S\alpha_g}{t_g} \tag{24}$$

$$\textit{Average heat generation in PV},\ \dot{Q}_{cell} = \frac{S\tau_g\alpha_{cell}(1-\eta_{cell})}{t_{cell}} \tag{25}$$

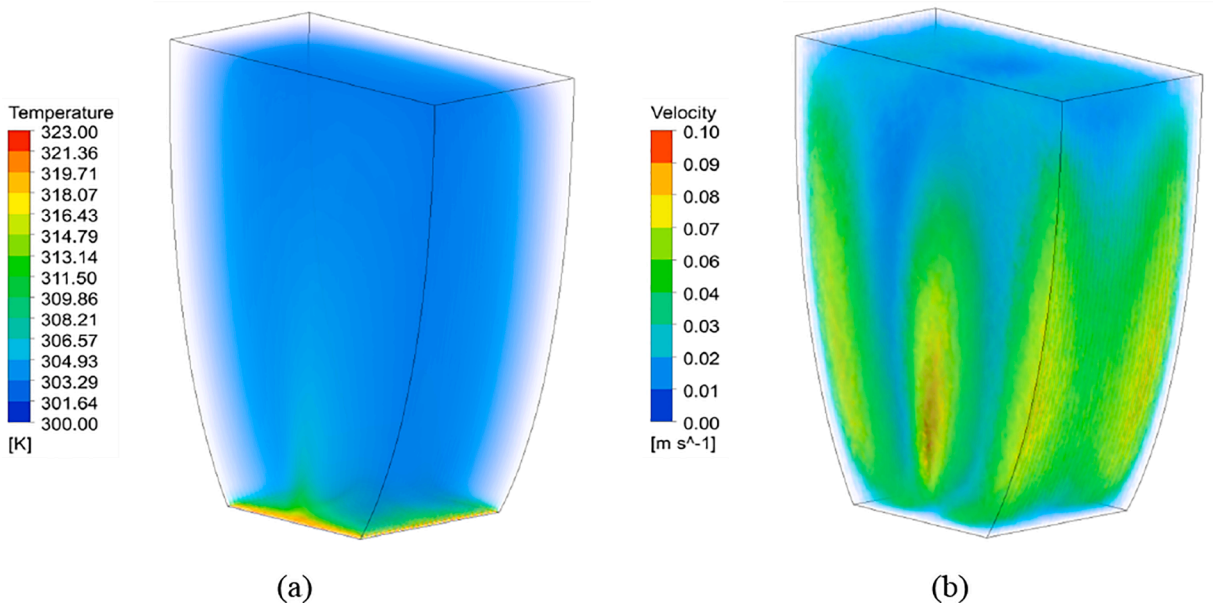

Fig. 16. 3-D numerical modeling of 2× -CPC: (a) Temperature field (b) Velocity field [59].

Table 7
Regression variable values.

Variable	Value
C_1	31.0750
C_2	1.7352
C_3	1.0993
C_4	1.0744
C_5	0.0208
C_6	−0.0908

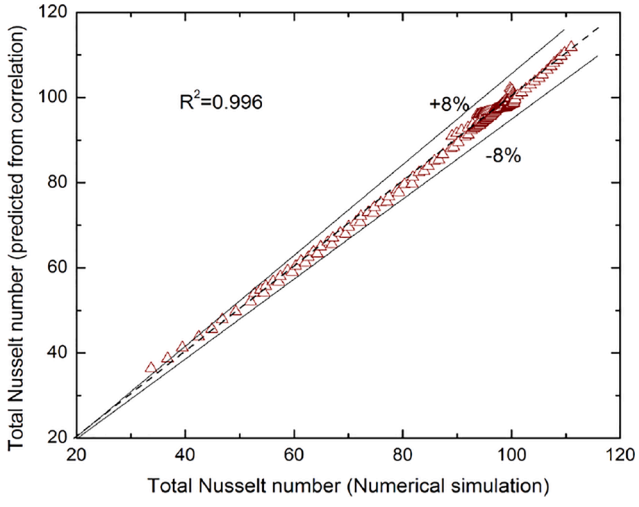

Fig. 17. Parity plot of average total Nusselt number for heat loss from the absorber of CPC.

where S is the concentrated average heat flux available at the CPC's exit aperture, t_g is thickness of glass cover, t_{cell} is thickness of solar cell, α_g is absorptivity of glass cover, α_{cell} is absorptivity of solar cell, τ_g is transmissivity of glass cover, and η_{cell} is solar cell efficiency. In the case of system performance using non-uniform heat flux, the $\dot{Q}_{cell}$ is local volumetric heat generation and is calculated the same way as the average heat generation with the average heat flux replaced by local

Table 8
Input conditions on the experimental day [41].

Time (h)	Incident radiation (W/m^2)	Ambient temperature (K)	Wind velocity (m/s)	Inlet water temperature (K)
9	449	291.49	0.66	289.91
10	587	291.88	1.19	290.93
11	767	292.38	0.71	293.92
12	864	294.12	2.20	295.42
13	691	293.78	0.90	294.96

Table 9
Unglazed CPC: Simulated solar cell temperature using average and local heat flux and comparison of cell temperature with that of experiments in [41].

Time (h)	Experimental T_{cell} (K)	Numerical: Average heat flux		Numerical: Local heat flux	
		T_{cell} (K)	Deviation in T_{cell} (%)	T_{cell} (K)	Deviation in T_{cell} (%)
9	302.33	297.23	1.69	305.80	1.15
10	307.54	302.44	1.66	310.20	0.86
11	312.74	310.86	0.60	315.72	0.95
12	318.98	314.18	1.50	316.82	0.68
13	314.65	309.79	1.54	316.08	0.45

Table 10
Glazed CPC: Simulated solar cell temperature using average and local heat flux and comparison of cell temperature with that of experiments in [41].

Time (h)	Experimental T_{cell} (K)	Numerical: Average heat flux		Numerical: Local heat flux	
		T_{cell} (K)	Deviation in T_{cell} (%)	T_{cell} (K)	Deviation in T_{cell} (%)
9	302.33	297.74	1.52	306.63	1.40
10	310.11	303.27	2.21	311.48	0.44
11	316.35	311.66	1.48	316.80	0.14
12	318.98	316.20	0.87	319.23	0.08
13	312.59	310.70	0.60	317.42	1.52

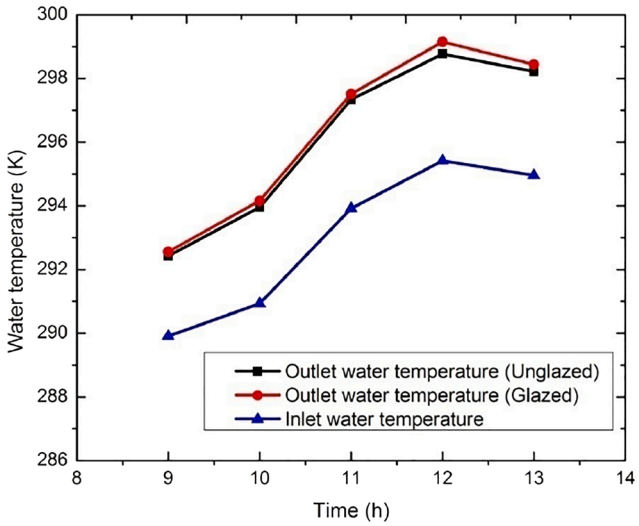

Fig. 18. Variation in outlet water temperature obtained from numerical analysis using non-uniform heat flux.

heat flux Eq. (26). The optical analysis of CPC gives local heat flux at discrete points on the absorber with which local heat generation is calculated while modeling the system performance under non-uniform heat flux. The absorber surface is resolved into 400 equally spaced data points. The procedure for mapping the non-uniform heat generation onto the solar cells [70] is given in the Appendix.

$$\textit{Local heat generation in PV},\ \sum_{i=1}^{400}\dot{Q}_{cell,i}=\sum_{i=1}^{400}\frac{S_i\tau_g\alpha_{cell}\left(1-\eta_{cell,i}\right)}{t_{cell}} \tag{26}$$

The top heat loss coefficient of the glazed system is calculated for the assumed glass cover temperature using Eq. (35). With this calculated initial heat generation and top heat loss coefficient, the governing equations are solved to obtain the new temperature values. The solar cell heat generation and top heat loss coefficient are updated for the succeeding iteration with the new solar cell and glass cover temperatures. The iterations are continued till the temperature difference between the two successive iterations falls below 0.001 °C.

In the case of an unglazed CPC system, the top convective heat loss coefficient is a function of external wind velocity. The top convective and radiation heat loss are defined separately (Fig. 10a). The iterative procedure adopted to calculate the solar cell heat generation is the same as described before for the glazed CPC system. The numerical methodology used for modeling the unglazed CPC PV/T system can be found in Fig. 4 of previous work [60]. The ANSYS Fluent finite volume solver discretizes the non-linear governing equations in to a set of algebraic equations for solving. While the discretization of momentum, energy, and user-defined scalar (UDS) is performed using a second-order upwind scheme, the pressure discretization is done using PRESTO. The pressure–velocity coupling is achieved using the SIMPLE scheme. The nonlinear coupled governing equations are solved till the residuals for velocity, continuity, and momentum reach 1×10^{-6}.

3.2.3. Meshing

The physical domain taken for thermal analysis is only the photovoltaic–thermal collector without the concentrator. The heat flux input to the model is the concentrated heat flux obtained from the optical analysis of CPC. The heat loss inside the CPC is calculated separately and is given as input to the model. The use of concentrated heat flux and top heat loss coefficient from external sources reduces the complexity of the domain by eliminating the concentrator and associated meshing. The system is modeled in the laminar flow regime and hence there is no requirement of special near-wall treatment. ANSYS meshing is used to generate the structured hexahedral elements for the PV/T collector. The PV/T layers are too thin and hence edge sizing of a suitable number of divisions is used at these fine layers to generate sufficient elements. The mesh relevance center is set to maximum and finer. The resultant mesh obtained by reducing the global element size and edge sizing is given in Fig. 13. The element size chosen for the meshing is 4.50×10^{-4} m. After element sizing and appropriate edge sizing on the glass cover, PV layer, and Tedlar, a total of 37,245,710 elements were generated in the computational domain. The average skewness of elements in the whole

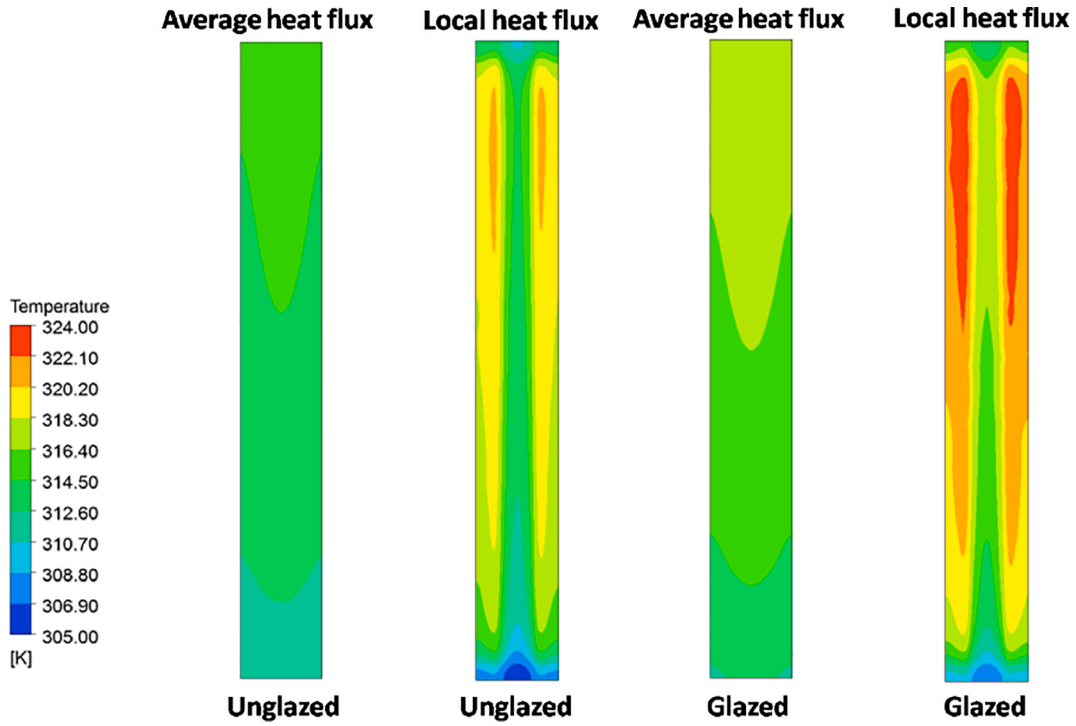

Fig. 19. Temperature contour of PV using average and non uniform heat flux at noon.

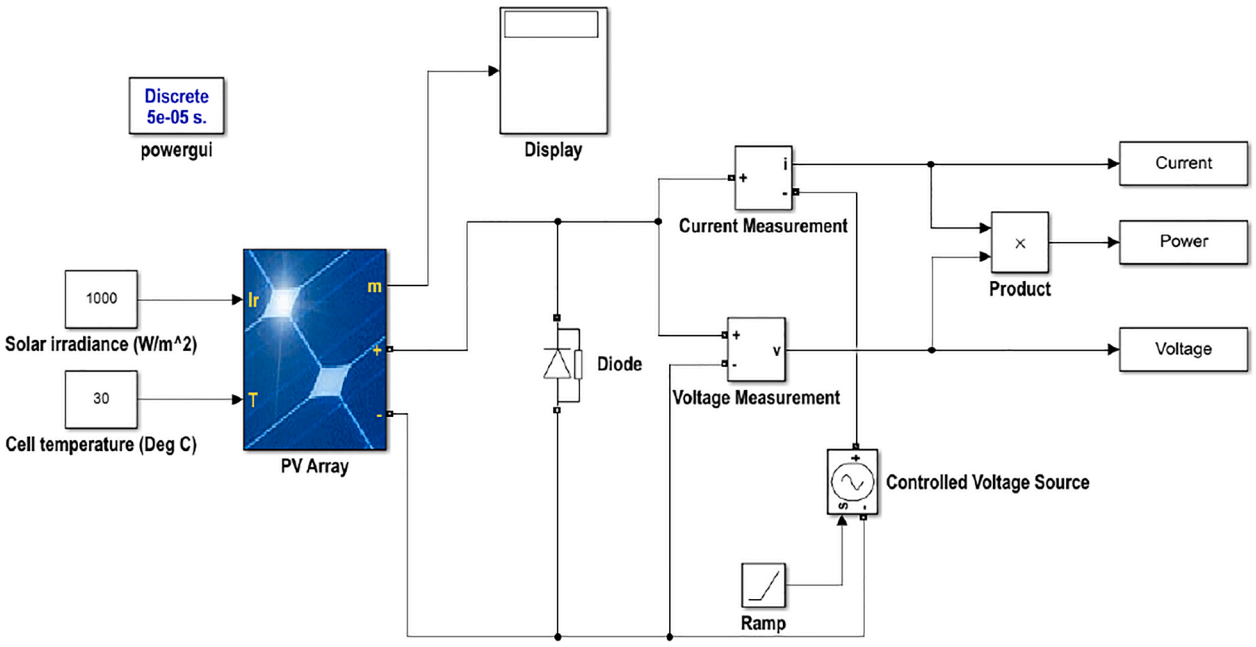

Fig. 20. Matlab/Simulink network for the simulation of electrical power from solar PV cell.

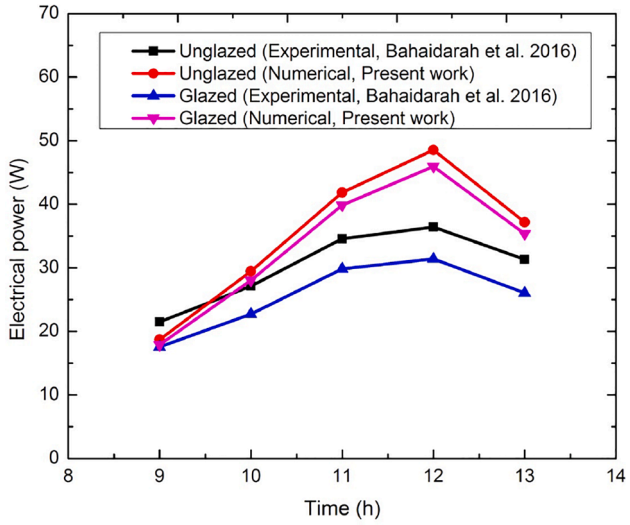

Fig. 21. Electrical power output from unglazed and glazed CPC-PV/T system.

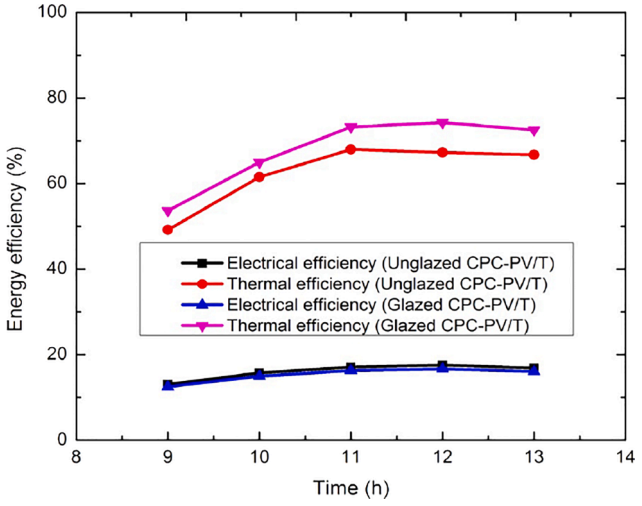

Fig. 22. Electrical and thermal energy efficiency of the CPC-PV/T system.

domain was 2.4×10^{-2}. The average aspect ratio of elements in the entire domain was 1.1. The average element quality in the entire domain was 0.97, which provided an excellent mesh quality for the computational domain. The computational domain and the corresponding meshing used for analysis of both the glazed and unglazed CPC-PV/T system is the same.

3.2.4. Boundary conditions

The heat transfer in PV/T is modeled by defining the heat flux entering the system and the heat loss from the exterior of the domain to the environment. The surface heat flux cannot be employed as a boundary condition since the solar PV is sandwiched between the glass cover and the Tedlar; instead, internal volumetric heat generation is used to describe the heat generated at the PV (Eq. (25)). The details of the boundary conditions in the computational domain are given in Fig. 10. The top surface of the glass cover is utilized to specify the heat loss coefficient, and hence the heat flux absorbed by the glass cover is also defined using heat generation (Eq. (24)). The presence of external wind allows for forced convection of heat from the exterior of the collector. Forced convection and surface radiation occur from the PV glass cover to the ambient. In the case of an unglazed CPC system, the convection and radiation heat losses are defined separately using the mixed boundary condition option available in FLUENT. The forced convection

Table 11
Simulated useful power output form CPC-PV/T system.

Time (h)	Unglazed CPC-PV/T useful power output (W)			Glazed CPC-PV/T useful power output (W)		
	Electrical	Thermal	Overall	Electrical	Thermal	Overall
9	18.7	0.04	18.74	17.91	0.08	17.99
10	29.44	0.39	29.83	28.04	0.49	28.53
11	41.86	2.54	44.40	39.85	2.74	42.59
12	48.55	2.27	50.82	45.93	2.69	48.62
13	37.17	2.09	39.26	35.36	2.32	37.68

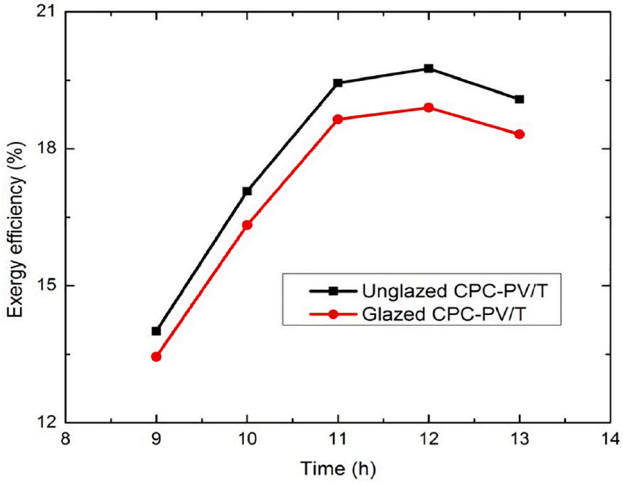

Fig. 23. Total exergy efficiency from unglazed and glazed CPC-PV/T systems.

of heat from the glass cover is simulated by defining a constant heat loss coefficient and external ambient temperature. The wind convection coefficient is calculated using Eq. (4). The surface radiation is simulated by defining external surface emissivity and sky temperature [65]. In the case of glazed CPC, the total heat loss coefficient from the glass cover to ambient through the glazing is obtained using the proposed correlation (described later in section 4.2.1). Zero heat flux is imposed at the sides and bottom of the collector as the side and bottom losses are small and are neglected. The fluid flow in the cooling tube is simulated by defining the inlet water temperature, flow rate, and outlet pressure. As described earlier, the flow is assumed to be fully developed and laminar, and hence a constant velocity is defined at the inlet of the cooling tube. The walls adjacent to the fluid domain are subjected to a no-slip boundary condition.

3.2.5. Mesh independent study

For any numerical modeling, it is required that the results are independent of grid resolution. The grid size is crucial since it impacts the accuracy of the result as well as the amount of time it takes to compute. It is necessary to fix the grid size that produces sufficiently accurate results, so we can preclude finer grids that involve increased computational time. Here, the grid sensitivity study is done by progressively reducing the global element size and computing the average solar cell temperature. The mesh study is done for an unglazed system at input conditions: $Q_i = 586.56$ W/m^2, $T_{amb} = 291.88$ K, $T_{in} = 290.93$ K and $V_w = 1.19$ m/s. It can be seen that as the element size is reduced, the average cell temperature declines at first, and then stabilizes. Table 3 shows the deviation in solar cell temperature obtained for various element sizes (first iteration result). Based on this data, the element size that is optimum for our thermal modeling of the concentrated PV/T system is 4.50×10^{-4} m.

3.3. Electrical model

The concentrated radiation from the optical model and the average solar cell temperature from the thermal model are imparted to the electrical model to obtain the electrical power output. The electrical characteristics of the solar cell considered are given in Table 4. The PV string consists of 8 mono-crystalline solar cells connected in series. The dimension of each cell is 125 mm $\times$ 125 mm. The electrical modeling is done in MATLAB Simulink. The irradiance and cell temperature-dependent electrical power output of the PV model is obtained using a five parameter electrical model. The conventional single diode model of solar cell with a series resistance and shunt resistance is considered for the analysis. The single diode equivalent circuit of a solar cell with series and shunt resistance is given in Fig. 14. Details of the electrical modeling of PV can be found in [71]. Current from the PV cell as a function of light generated current (I_{pv}) and saturation current (I_o) is given by Eq. (27).

$$\textit{Photovoltaic current, } I = I_{PV} - I_0\left[exp\left(\frac{V+IR_s}{V_t a}\right) - 1\right] - \left(\frac{V+IR_s}{R_p}\right) \tag{27}$$

3.4. Overall system output

The electrical power generated by the solar cells is obtained by multiplying the voltage and current corresponding to the maximum power point of the IV curve. The electrical energy efficiency and thermal energy efficiency of the CPV/T collector can be calculated by Eq. (28)-(29) [72]. The term S in Eq. (28) is the concentrated radiation available at the exit aperture of CPC and the term A_r is the receiver area of the module. The solar PV/T collector produces both electrical and thermal power output, and using the concept of energetic evaluation of the PV/T collector is inappropriate since the nature of the energies obtained are different. Electrical energy can be completely converted to useful work independent of ambient conditions. Whereas, thermal energy cannot be completely transformed into useful work as it depends on a temperature difference between the heat source and sink. It is appropriate to use the concept of exergy theorem while evaluating the performance of solar PV/T collectors that take the nature of energy into account. Electrical energy has the same exergy as it can be fully converted into work Eq. (30). The thermal energy cannot be fully made available for useful work as the maximum available energy is restricted by ambient conditions. The overall useful energy gain is the sum of useful thermal gain and electrical gain Eq. (32) [73].

$$\textit{Electrical efficiency of the CPV/T module, } \eta_{ele} = \frac{IV}{SA_r} \tag{28}$$

$$\textit{Thermal efficiency of the CPV/T module, } \eta_{th} = \frac{\dot{m}C_p(T_{out} - T_{in})}{SA_r} \tag{29}$$

$$\textit{Electrical exergy, } Q_{u,ele} = IV \tag{30}$$

$$\textit{Thermal exergy, } Q_{u,th} = \dot{m}C_p\left[(T_{out} - T_{in}) - (T_{amb} + 273)\ln\left(\frac{T_{out}+273}{T_{in}+273}\right)\right] \tag{31}$$

$$\textit{Overall exergy of the CPV/T system, } Q_{u,tot} = Q_{u,ele} + Q_{u,th} \tag{32}$$

$$\textit{Exergy of incident radiation, } Q_{u,in} = SA_r\left[1 - \frac{4}{3}\left(\frac{T_{amb}}{T_{sun}}\right) + \frac{1}{3}\left(\frac{T_{amb}}{T_{sun}}\right)^4\right] \tag{33}$$

$$\textit{Exergy efficiency of the CPV/T system, } \eta_{u,tot} = \frac{Q_{u,tot}}{Q_{u,in}} \tag{34}$$

4. Results and discussion

Using the integrated optical-thermal and electrical model, the performance of the CPC-PV/T system is evaluated under uniform and non-uniform heat flux input. The obtained results are validated against experimental results reported in [41]. Bahaidarah et al. have done experimental studies on both the glazed and unglazed CPC-PV/T systems installed at Dhahran (26.23° N, 50.04° E), Saudi Arabia [41].

4.1. Optical analysis

To develop a coupled optical-thermal model, the flux available at the absorber of both glazed and unglazed CPC at various time instances on an experimental day is required. Hence, optical analysis is done for the

CPC corresponding to the input conditions on an experimental day (4th Feb) mentioned in the literature [41]. Ideally, the DNI and angle of incident variation in a day resemble a half-sine wave, and hence the numerical simulations are done for one half of the day. For the other half, it is symmetric about noon. The CPC-PV/T system is oriented in the E-W direction and is tilted about the horizontal by 41.5°. The angle at which solar radiation is incident on the inlet aperture of CPC is calculated using the sun-angle relationships described earlier in section 3.1.2. The optical analysis is done for various time instances by changing the DNI and the angle of incidence. The results of both the unglazed and glazed CPC obtained from ray-tracing are given in Tables 5 and 6. The corresponding local flux profile at the absorber of unglazed CPC is given in Fig. 15. For identification purposes, the angle of incidence is given a positive sign for incidences before solar noon and a negative sign for incidences after solar noon. Due to the angular movement of the sun across the sky in a day, the angle of incidence is maximum in the morning, reduces to a minimum at noon, and again increases in the evening. The optical efficiency of an unglazed CPC is better than a glazed CPC. The absorption of incident light at the glazing reduces the optical efficiency of the glazed CPC system. From Fig. 15, it can be seen that for the CPC oriented in the E-W direction, the magnitude of the heat flux varies throughout the day but the location of peak flux on the absorber remains the same throughout the day. The location of maximum heat flux occurs at ± 30 mm (width of absorber). The maximum optical efficiency of unglazed CPC is 95.05% and that of glazed CPC is 90.43%. The maximum optical efficiency is obtained at noon due to the low angle of incidence (-1.81°). The average and local heat flux obtained from the ray-tracing is mapped onto the solar cell for obtaining the thermal performance of PV/T.

4.2. Thermal analysis of CPC-PV/T system

4.2.1. Development of correlation for total heat loss from the absorber of glazed CPC

The heat loss inside the glazed CPC is due to natural convection caused by differential heating of air between the hot absorber and cold glazing. Previously the authors have done extensive work on modeling coupled convection and radiation inside a CPC of 2× concentration. The temperature contour showing the rise of thermal plume and the bicellular flow fields are given in Fig. 16. The results of which can be found in [59] wherein the performance of the CPC is modeled in 3D and compared with experimental results available in the literature. The heat loss in CPC is modeled for different absorber temperature, ambient temperature, absorber emissivity, external heat loss coefficient, truncation and angular orientation. The results of which are extended here to propose a correlation for the average total Nusselt number for heat loss in CPC. Estimation of average total Nusselt number is done by non-linear regression analysis with 207 data points using DataFit 9.1. To obtain the total Nusselt number as a function of several independent parameters a user-defined function of the form given below is used.

$$y = C_1 x_1^{C_2} x_2^{C_3} x_3^{C_4} x_4^{C_5} x_5^{C_6}$$

where C_1 to C_6 are correlation constants obtained from regression analysis (Table 7)

x_1 to x_5 are non dimensional independent parameters that influence the dependent parameter y.

The parity plot showing the average total Nusselt number obtained from numerical simulation and that from developed correlation is given in Fig. 17. The result shows excellent prediction with correlation coefficient 0.996 and error band ±8%. The correlation for average total Nusselt number as a function of absorber temperature, ambient temperature, absorber emissivity, external heat loss coefficient, truncation and angular orientation with air as working medium is given in Eq. (35) and their correlation constants are given in Table 7.

$$\overline{Nu_{tot}} = C_1 \left(\frac{T_{abs}}{T_{amb}}\right)^{C_2} \left(\frac{H_t}{W_{gz}}\right)^{C_3} (1+\varepsilon)^{C_4} \left(\frac{h_{ext} H_t}{\lambda}\right)^{C_5} (cos\psi)^{C_6} \quad (35)$$

For the range of parameters: 313 K ≤ T_{abs} ≤ 353 K; 294 K ≤ T_{amb} ≤ 306 K; 0.05 ≤ ε ≤ 0.8; 0° ≤ Ψ ≤ 60°; 5 W/m^2 -K ≤ h_{ext} ≤ 35 W/m^2 -K.

$$\textit{Total heat loss coefficient from the CPC is, } h_{tot} = \frac{\overline{Nu_{tot}}\lambda}{H_t} \quad (36)$$

where λ is thermal conductivity of air computed at average temperature of absorber and ambient, H is height of CPC, H_t is height of CPC after truncation, W_{gz} is width of glazing, h_{ext} is external convective heat loss coefficient, and Ψ is tilt angle of the panel. The proposed correlation is used to calculate the top heat loss coefficient of glazed CPC by assuming an initial value for the absorber temperature. While modeling the glazed CPC system, the heat loss is between cover glass and glazing and hence absorber temperature in Eq. (35) is glass cover temperature and emissivity is glass cover emissivity (0.93). For the system modeled here, the design parameters are H_t = 253 mm, W_{gz} = 314.5 mm and Ψ = 41.5°. The term h_{ext} is external wind loss coefficient and is calculated using Eq. (4).

4.2.2. Thermal analysis

The thermal modeling of the PV/T collector takes solar heat load (part of incident energy that is converted to heat after photovoltaic conversion) as input to determine the temperature distribution in the collector. The modeling is done for both the glazed and unglazed CPC-PV/T system using the iterative procedure described before. The incident radiation, ambient temperature, wind velocity, and inlet water temperature measured on an experimental day at Dhahran is given in Table 8 [41]. Tables 9 and 10 show the simulated and experimental results along with the deviation obtained in average solar cell temperature. The solar cell temperature reaches its maximum at noon due to maximum incident radiation at noon. The modeling shows excellent prediction with a maximum deviation in cell temperature of less than 3%. Also, the deviation in cell temperature obtained using non-uniform local heat flux is found to be lower than the deviation obtained when using average heat flux. The results show the need for a local heat flux profile in moving closer towards the accurate modeling of a concentrated PV/T collector. The heat from the solar cell is recovered by water flowing in the duct placed underneath the solar cell. The modeling is done for the flow rate of 1 LPM and the outlet water temperature obtained from both the unglazed and glazed CPC-PV/T is given in Fig. 18. The outlet water temperature obtained from the glazed CPC-PV/T system is higher than the water temperature obtained from the unglazed CPC-PV/T system.

The temperature values show that the temperature of the glazed CPC-PV/T system is more than the unglazed CPC-PV/T system. This is because the glazing on top acts as a barrier for heat loss from the top surface of the solar cell whereas in the case of an unglazed CPC system, the top heat loss is high due to external forced convection by the wind. The temperature contour of PV from both glazed and unglazed CPC systems taken at noon is shown in Fig. 19. The temperature profiles are different when using average heat flux and when using non-uniform heat flux. It can be seen that the temperature of PV increases along the length this is because the water flowing underneath the panel is removing the heat as it flows along the collector length.

4.3. Electrical analysis

The electrical modeling is done in MATLAB Simulink. The electrical model for the solar cell is represented in the form of mathematical equations. The five parameters of the electrical model are light generated current, diode reverse-saturation current, series resistance, shunt resistance and diode ideality factor. Details of the electrical modeling of PV can be found in [71]. The five-parameter electrical model takes

average heat flux and average solar cell temperature (obtained from the non-uniform heat flux case) as inputs to produce the electrical power output. The Simulink network for the solar PV module is given in Fig. 20. The block parameters for the PV array are given in Table 4, with the number of cells in series taken as eight. The Simulink model takes solar irradiance and cell temperature as input and gives current, voltage and power produced from the PV array. The point corresponding to maximum power from the P-V curve is taken as the power output from the PV array. The electrical power output obtained from the electrical modeling of solar cells is given in Fig. 21. It can be seen that the electrical power output from the unglazed PV/T system is more because the cell temperature in the unglazed CPC-PV/T system is lower than the cell temperature of the glazed CPC-PV/T system. The maximum electrical power obtained from the unglazed CPC-PV/T system is 48.55 W at noon. And the maximum electrical power obtained from glazed CPC-PV/T system is 45.93 W at noon. The deviation in electrical power between the simulated and experimental values is 8%–33% in the unglazed system and 2%-45% in the glazed system.

4.4. Overall output from CPC-PV/T system

The electrical and thermal energy efficiency calculated for the unglazed and glazed CPC-PV/T systems on the experimental day is given in Fig. 22. The electrical efficiency of the unglazed CPC-PV/T system is higher than that of the glazed CPC-PV/T system, as can be observed. The thermal energy efficiency of the glazed CPC-PV/T system is better than that of the unglazed CPC-PV/T system. The maximum electrical efficiency produced by the unglazed and glazed systems is 17.61% and 16.66%. The overall output obtained from the system based on the available energy is also given in Table 11. It can be concluded that the unglazed CPC-PV/T system produces maximum overall output. The thermal power reported in Table 11 is the useful thermal power that is calculated using Eq. (31). The total useful power is the sum of electrical power and useful thermal power. Both electrical power and thermal power are found to increase with an increase in incident radiation. The maximum power is produced around noon, during which the incident radiation is 864 W/m^2 and the angle of incidence is −1.81°. The maximum overall useful power from the unglazed and glazed CPC-PV/T systems is 50.82 W and 48.62 W, respectively. The total exergy efficiency obtained from the unglazed and glazed CPC-PV/T system for the input conditions on the experimental day is given in Fig. 23. The total exergy efficiency of the CPC-PV/T collector is calculated using Eq. (34) by taking the sun's temperature as 5760 K. The total exergy efficiency of the unglazed CPC-PV/T system is 14.02%-19.75% and the total exergy efficiency of the glazed CPC-PV/T system is 13.44%-18.89%. The total exergy efficiency obtained from the unglazed CPC-PV/T system is higher than the exergy efficiency obtained from the glazed CPC-PV/T system.

5. Conclusions

An integrated multi-physics simulation is done combining ray tracing, fluid flow, heat transfer, and electrical model to obtain the performance of concentrated PV/T system. The optical efficiency study shows that the efficiency of unglazed CPC is more than the efficiency of glazed CPC. The concentrated heat flux obtained for various angles of incidence is mapped on the solar cell to obtain its thermal performance. The obtained cell temperatures are compared with experimental results available in the literature. The results show that the solar cell temperature obtained when using the local heat flux profile yields more accurate results than when using average heat flux. The maximum deviation in cell temperature when using local heat flux is 1.52%. For the system conditions modeled here, the temperature of the glazed CPC-PV/T system is more than the temperature of the unglazed CPC-PV/T system by around 1 °C. The temperature contours of PV clearly depict the critical need for local heat flux in predicting the exact temperature profile of PV. The thermal output from the system is too low and is due to a high flow rate that was intended to reduce the operating temperature of PV. The power output from the system shows that the unglazed CPC-PV/T produces high electrical and overall system output than the glazed CPC-PV/T system.

A correlation is proposed for the heat loss in a glazed CPC as a function of absorber temperature, ambient temperature, absorber emissivity, external heat loss coefficient, truncation, and angular orientation. The accuracy of the model can be further improved by using local heat flux and local temperature in electrical modeling. This multi-physics coupled model gives an accurate performance of the CPV/T system so that system modification can be simulated when designing the collector for attaining temperature homogeneity.

CRediT authorship contribution statement

Anandhi Parthiban: Data curation, Investigation, Methodology, Software, Validation, Writing – original draft. **T.K. Mallick:** Conceptualization, Formal analysis, Funding acquisition, Investigation, Methodology, Project administration, Resources, Supervision, Visualization, Writing – original draft. **K.S. Reddy:** Conceptualization, Formal analysis, Investigation, Supervision, Visualization, Resources, Supervision, Writing – original draft.

Declaration of Competing Interest

The authors declare that they have no known competing financial interests or personal relationships that could have appeared to influence the work reported in this paper.

Acknowledgements

The financial support provided by the Department of Science and Technology, Government of India through the project, DST/TM/SERI/C278(C) is duly acknowledged. We acknowledge the use of the computing resources at HPCE, IIT Madras.

Appendix

A.1 Procedure for mapping the concentrated heat flux obtained from ray tracing

The local heat flux obtained from the ray tracing analysis is mapped on to the solar cell using the simple procedure described below.

1. Compute the local heat generation in solar cell using the local heat flux obtained from SolTtrace. The local heat generation in solar cell is calculated using the formula given below. Store the calculated heat generation values along with x, y and z coordinates in a file with extension *.ip

$$\textit{Local heat generation in PV},\ \sum_{i=1}^{400} \dot{Q}_{cell,i} = \sum_{i=1}^{400} \frac{S_i \tau_g \alpha_{cell}\left(1-\eta_{cell,i}\right)}{t_{cell}}$$

2. Compile the udf file (*.c). Build and load the libduf file in fluent.
3. Set the required number of uds and udm (uds-0 and udm-0) and assign it to the required cell zone (solar cell)
4. Once the required number of uds and udm is set, initialize the solution and patch zero value to uds-0 and udm-0 in the selected cell zone.
5. Interpolate *.ip file at the selected cell zone to uds-0. Copy the contents in uds-0 to udm-0 using execute on demand command.
6. Define materials, boundary conditions, solver and residuals.
7. Initialize the solution using hybrid initialization. Upon initialization, the uds-0 and udm-0 is reset to zero so there is a need to again read the *ip file in uds-0 and copy its content to udm-0 before calculating the solution.

A.2 Optical analysis of CPC in N-S orientation

Fig. A1

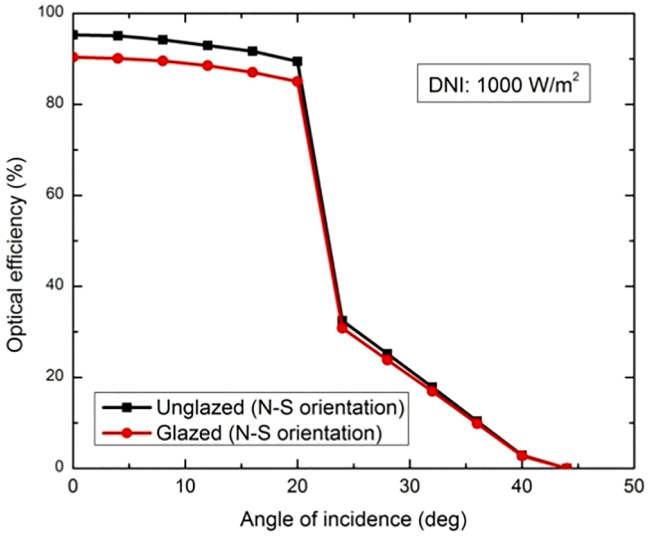

Fig. A1. Optical analysis of CPC in N-S orientation.

A.3 Temperature contour of PV using average and non uniform heat flux.

Fig. A2

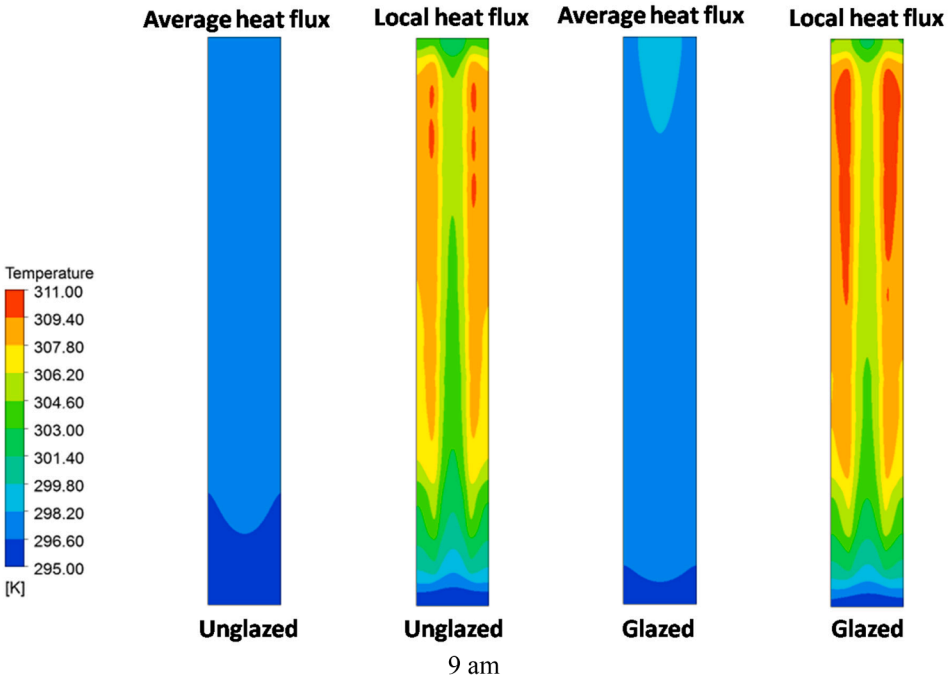

Fig. A2. Temperature contour of PV using average and non uniform heat flux.

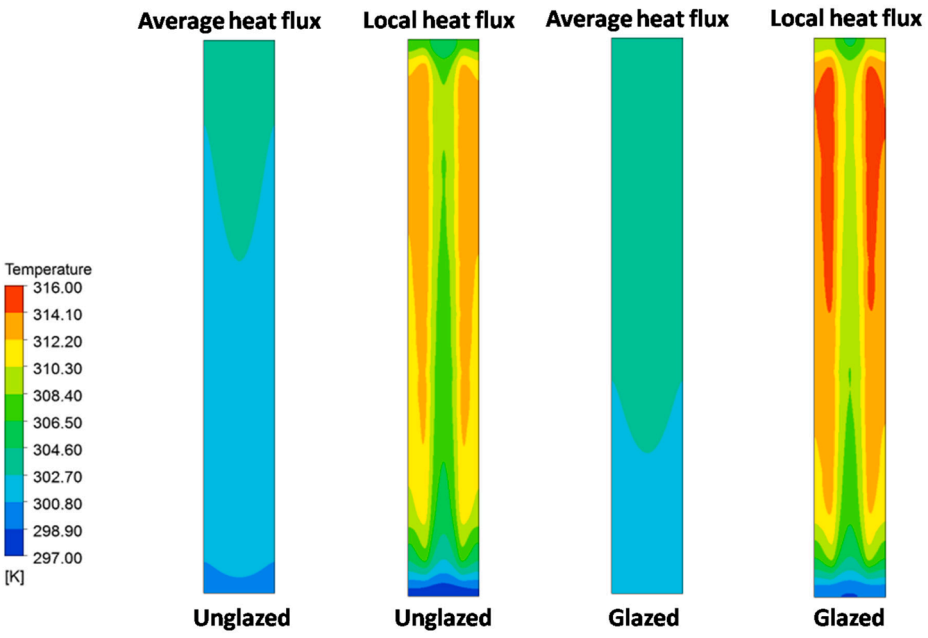

Fig. A2. (*continued*).

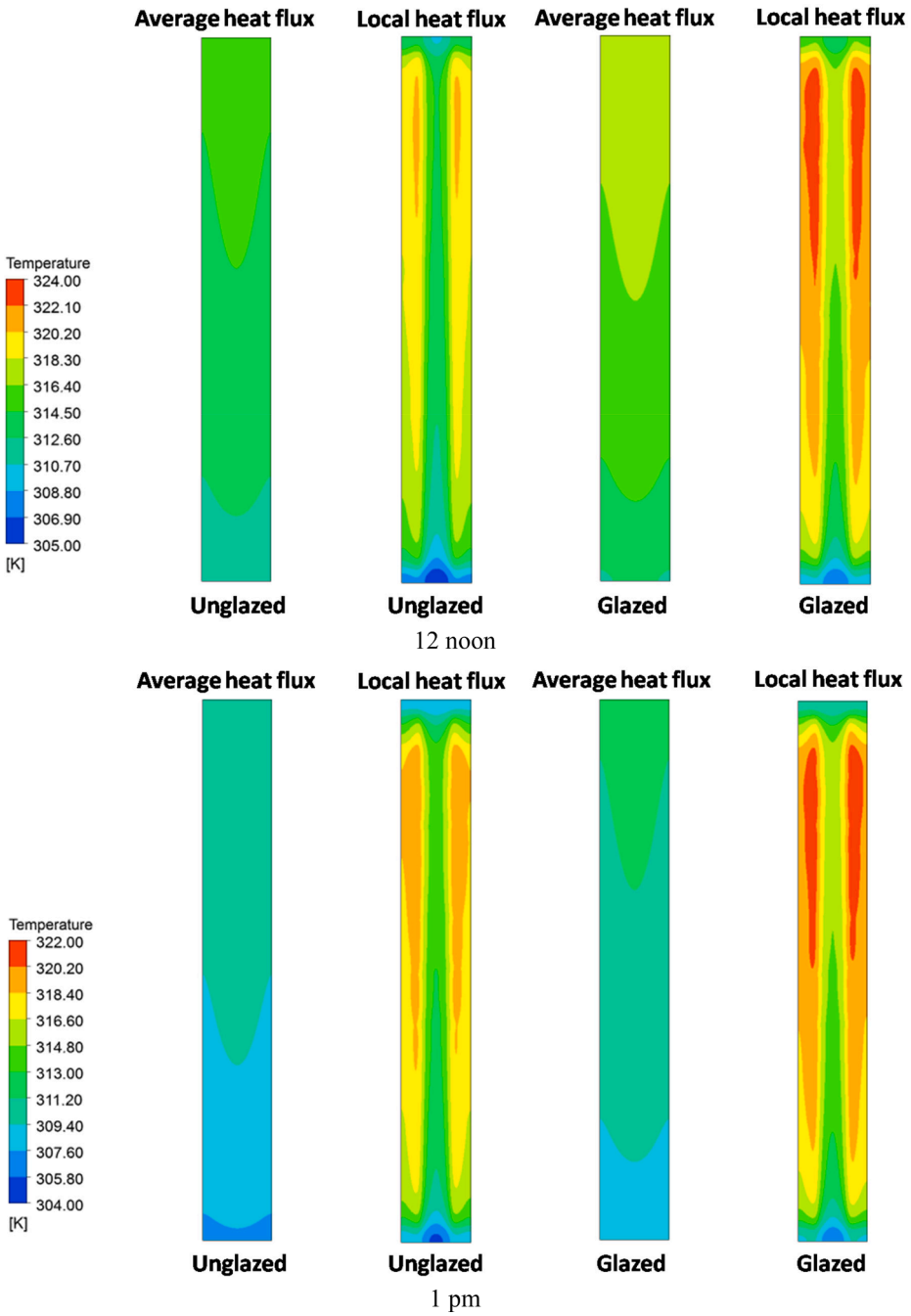

Fig. A2. (*continued*).

A.4 Electrical modeling of solar cell [71]

Current from the PV cell as a function of light generated current (I_{pv}) and saturation current (I_o) is given by

$$Photovoltaic\ current,\ I = I_{PV} - I_0\left[exp\left(\frac{V+IR_s}{V_t a}\right) - 1\right] - \left(\frac{V+IR_s}{R_p}\right)$$

where I_{PV} and I_o are the photovoltaic and reverse saturation currents, respectively, of the module. The thermal voltage of the module with (N_s) number of cells connected in series is represented by

$$Thermal\ voltage\ of\ the\ module, V_t = \frac{N_s KT}{q}$$

In the above equation, K stands for Boltzmann constant (1.3806×10^{-23} J/K), while q stands for electron charge (1.6021×10^{-19}C). The diode saturation current I_o and its dependence on the temperature are expressed as

$$\textit{Diode saturation current},\ I_0 = I_{0,n}\left(\frac{T_n}{T}\right)^3 exp\left[\frac{qE_g}{aK}\left(\frac{1}{T_n}-\frac{1}{T}\right)\right]$$

Where E_g is the band gap energy of semiconductor, $E_g = 1.12$ eV for polycrystalline silicon solar cell at 25 °C, $I_{0,n}$is the nominal saturation current and is given by

$$\textit{Nominal saturation current},\ I_{0,n} = \frac{I_{sc,n}}{exp\left(\frac{V_{oc,n}}{aV_{t,n}}\right)-1}$$

with $V_{t,n}$being the thermal voltage of N_s series connected cells at the nominal temperature T_n. The light-generated current of the PV cell depends linearly on the solar irradiation and is also influenced by the temperature according to the following equation

$$\textit{Light}-\textit{generated current of the PV cell},\ I_{PV} = \left(I_{PV,n} + K_I\Delta T\right)\frac{Q}{Q_n}$$

where $I_{pv,n}$ is the light-generated current at the nominal condition , $\Delta T = T - T_n$ (T and T_n being the actual and nominal temperatures, respectively), Q is the irradiation on the device surface, and Q_n is the nominal irradiation. The nominal light-generated current $I_{pv,n}$ can be expressed with accurate equation of the following

$$\textit{Nominal light}-\textit{generated current},\ I_{PV,n} = \frac{R_p + R_s}{R_p} I_{sc,n}$$

The current from the photovoltaic module can be obtained by substituting photovoltaic current (I_{pv}), reverse saturation current (I_o), series resistance (R_s), and shunt resistance (R_p) in Eq. (27).

References

[1] Siddiqui M, Arif A. Electrical, thermal and structural performance of a cooled PV module: Transient analysis using a multiphysics model. Appl Energy 2013;112:300–12. https://doi.org/10.1016/j.apenergy.2013.06.030.

[2] Zaraket J, Khalil T, Aillerie M, Vokas GA, Salame C. The Effect of Electrical stress under temperature in the characteristics of PV Solar Modules. Energy Procedia 2017;119:579–601. https://doi.org/10.1016/j.egypro.2017.07.083.

[3] Hollick JC. Solar cogeneration panels. Renewable Energy 1998;15(1-4):195–200. https://doi.org/10.1016/S0960-1481(98)00154-2.

[4] George M, Pandey A, Rahim NA, Tyagi V, Shahabuddin S, Saidur R. Concentrated photovoltaic thermal systems: A component-by-component view on the developments in the design, heat transfer medium and applications. Energy Convers Manage 2019;186:15–41. https://doi.org/10.1016/j.enconman.2019.02.052.

[5] Siecker J, Kusakana K, Numbi B. A review of solar photovoltaic systems cooling technologies. Renew Sustain Energy Rev 2017;79:192–203. https://doi.org/10.1016/j.rser.2017.05.053.

[6] Nasef HA, Nada SA, Hassan H. Integrative passive and active cooling system using PCM and nanofluid for thermal regulation of concentrated photovoltaic solar cells. Energy Convers Manage 2019;199:112065. https://doi.org/10.1016/j.enconman.2019.112065.

[7] Yazdanifard F, Ameri M, Taylor RA. Numerical modeling of a concentrated photovoltaic/thermal system which utilizes a PCM and nanofluid spectral splitting. Energy Convers Manage 2020;215:112927. https://doi.org/10.1016/j.enconman.2020.112927.

[8] Nižetić S, Papadopoulos A, Giama E. Comprehensive analysis and general economic-environmental evaluation of cooling techniques for photovoltaic panels, Part I: Passive cooling techniques. Energy Convers Manage 2017;149:334–54. https://doi.org/10.1016/j.enconman.2017.07.022.

[9] Grubišić-Čabo F, Nižetić S, Čoko D, Kragić IM, Papadopoulos A. Experimental investigation of the passive cooled free-standing photovoltaic panel with fixed aluminum fins on the backside surface. J Cleaner Prod 2018;176:119–29. https://doi.org/10.1016/j.jclepro.2017.12.149.

[10] Waqas A, Ji J. Thermal management of conventional PV panel using PCM with movable shutters – A numerical study. Sol Energy 2017;158:797–807. https://doi.org/10.1016/j.solener.2017.10.050.

[11] Zarma I, Ahmed M, Ookawara S. Enhancing the performance of concentrator photovoltaic systems using Nanoparticle-phase change material heat sinks. Energy Convers Manage 2019;179:229–42. https://doi.org/10.1016/j.enconman.2018.10.055.

[12] Abd-Elhady M, Serag Z, Kandil H. An innovative solution to the overheating problem of PV panels. Energy Convers Manage 2018;157:452–9. https://doi.org/10.1016/j.enconman.2017.12.017.

[13] Xin G, Wang Y, Sun Y, Huang Q, Zhu L. Experimental study of liquid-immersion III–V multi-junction solar cells with dimethyl silicon oil under high concentrations. Energy Convers Manage 2015;94:169–77. https://doi.org/10.1016/j.enconman.2015.01.063.

[14] Sato D, Yamada N. Review of photovoltaic module cooling methods and performance evaluation of the radiative cooling method. Renew Sustain Energy Rev 2019;104:151–66. https://doi.org/10.1016/j.rser.2018.12.051.

[15] Tonui JK, Tripanagnostopoulos Y. Air-cooled PV/T solar collectors with low cost performance improvements. Sol Energy 2007;81(4):498–511. https://doi.org/10.1016/j.solener.2006.08.002.

[16] Nižetić S, Giama E, Papadopoulos A. Comprehensive analysis and general economic-environmental evaluation of cooling techniques for photovoltaic panels, Part II: Active cooling techniques. Energy Convers Manage 2018;155:301–23. https://doi.org/10.1016/j.enconman.2017.10.071.

[17] Ebaid M, Ghrair A, Al-Busoul M. Experimental investigation of cooling photovoltaic (PV) panels using (TiO 2) nanofluid in water -polyethylene glycol mixture and (Al 2 O3) nanofluid in water- cetyltrimethylammonium bromide mixture. Energy Convers Manage 2018;155:324–43. https://doi.org/10.1016/j.enconman.2017.10.074.

[18] Al-Waeli AH, Sopian K, Chaichan MT, Kazem HA, Hasan HA, Al-Shamani AN. An experimental investigation of SiC nanofluid as a base-fluid for a photovoltaic thermal PV/T system. Energy Convers Manage 2017;142:547–58. https://doi.org/10.1016/j.enconman.2017.03.076.

[19] Makki A, Omer S, Su Y, Sabir H. Numerical investigation of heat pipe-based photovoltaic–thermoelectric generator (HP-PV/TEG) hybrid system. Energy Convers Manage 2016;112:274–87. https://doi.org/10.1016/j.enconman.2015.12.069.

[20] Rahimi M, Valeh-E-Sheyda P, Parsamoghadam MA, Masahi MM, Alsairafi AA. Design of a self-adjusted jet impingement system for cooling of photovoltaic cells. Energy Convers Manage 2014;83:48–57. https://doi.org/10.1016/j.enconman.2014.03.053.

[21] Zsiborács H, Pályi B, Pintér G, Popp J, Balogh P, Gabnai Z, et al. Technical-economic study of cooled crystalline solar modules. Sol Energy 2016;140:227–35. https://doi.org/10.1016/j.solener.2016.11.009.

[22] Chen Y, Wang J, Ma C, Shi G. Multicriteria performance investigations of a hybrid ground source heat pump system integrated with concentrated photovoltaic thermal solar collectors. Energy Convers Manage 2019;197:111862. https://doi.org/10.1016/j.enconman.2019.111862.

[23] Bahaidarah HM. Experimental performance evaluation and modeling of jet impingement cooling for thermal management of photovoltaics. Sol Energy 2016;135:605–17. https://doi.org/10.1016/j.solener.2016.06.015.

[24] ROYNE A, DEY C, MILLS D. Cooling of photovoltaic cells under concentrated illumination: a critical review. Sol Energy Mater Sol Cells 2005;86(4):451–83. https://doi.org/10.1016/j.solmat.2004.09.003.

[25] Arcuri N, Reda F, Simone MD. Energy and thermo-fluid-dynamics evaluations of photovoltaic panels cooled by water and air. Sol Energy 2014;105:147–56. https://doi.org/10.1016/j.solener.2014.03.034.

[26] Gholami H, Sarwat A, Hosseinian H, Khalilnejad A. Evaluation of optimal dual axis concentrated photovoltaic thermal system with active ventilation using Frog Leap algorithm. Energy Convers Manage 2015;105:782–90. https://doi.org/10.1016/j.enconman.2015.08.033.

[27] Aldossary A, Mahmoud S, Al-Dadah R. Technical feasibility study of passive and active cooling for concentrator PV in harsh environment. Appl Therm Eng 2016;100:490–500. https://doi.org/10.1016/j.applthermaleng.2016.02.023.

[28] Bianchini A, Guzzini A, Pellegrini M, Saccani C. Photovoltaic/thermal (PV/T) solar system: Experimental measurements, performance analysis and economic assessment. Renewable Energy 2017;111:543–55. https://doi.org/10.1016/j.renene.2017.04.051.

[29] Cappelletti A, Nelli LC, Reatti A. Integration and architectural issues of a photovoltaic/thermal linear solar concentrator. Sol Energy 2018;169:362–73. https://doi.org/10.1016/j.solener.2018.05.013.

[30] Chen H, Ji J, Pei G, Yang J, Zhang Y. Experimental and numerical comparative investigation on a concentrating photovoltaic system. J Cleaner Prod 2018;174:1288–98. https://doi.org/10.1016/j.jclepro.2017.11.058.

[31] Hasan A, Sarwar J, Shah AH. Concentrated photovoltaic: A review of thermal aspects, challenges and opportunities. Renew Sustain Energy Rev 2018;94:835–52. https://doi.org/10.1016/j.rser.2018.06.014.

[32] Elsafi AM, Gandhidasan P. Comparative study of double-pass flat and compound parabolic concentrated photovoltaic–thermal systems with and without fins. Energy Convers Manage 2015;98:59–68. https://doi.org/10.1016/j.enconman.2015.03.084.

[33] Zhang G, Wei J, Wang Z, Xie H, Xi Y, Khalid M. Investigation into effects of non-uniform irradiance and photovoltaic temperature on performances of photovoltaic/thermal systems coupled with truncated compound parabolic concentrators. Appl Energy 2019;250:245–56. https://doi.org/10.1016/j.apenergy.2019.05.022.

[34] Baig H, Heasman KC, Mallick TK. Non-uniform illumination in concentrating solar cells. Renew Sustain Energy Rev 2012;16(8):5890–909. https://doi.org/10.1016/j.rser.2012.06.020.

[35] Rabl A. Optical and thermal properties of compound parabolic concentrators. Sol Energy 1976;18(6):497–511. https://doi.org/10.1016/0038-092X(76)90069-4.

[36] Guiqiang L, Gang P, Yuehong S, Jie J, Riffat SB. Experiment and simulation study on the flux distribution of lens-walled compound parabolic concentrator compared with mirror compound parabolic concentrator. Energy 2013;58:398–403. https://doi.org/10.1016/j.energy.2013.06.027.

[37] Paul DI. Optical performance analysis and design optimisation of multisectioned compound parabolic concentrators for photovoltaics application. Int J Energy Res 2019;43(1):358–78. https://doi.org/10.1002/er.v43.110.1002/er.4271.

[38] Xie H, Wei J, Wang Z, Yang G, Ma Q. Design and performance research on eliminating multiple reflections of solar radiation within compound parabolic concentrator (CPC) in hybrid CPV/T system. Sol Energy 2016;129:126–46. https://doi.org/10.1016/j.solener.2016.01.037.

[39] Chandan, Dey S, Kumar PS, Reddy K, Pesala B. Optical and electrical performance investigation of truncated 3X non-imaging low concentrating photovoltaic-thermal systems. Energy Conversion and Management 2020;220:113056. doi:10.1016/j.enconman.2020.113056.

[40] Baig H, Sarmah N, Heasman KC, Mallick TK. Numerical modelling and experimental validation of a low concentrating photovoltaic system. Sol Energy Mater Sol Cells 2013;113:201–19. https://doi.org/10.1016/j.solmat.2013.01.035.

[41] Bahaidarah HM, Gandhidasan P, Baloch AA, Tanweer B, Mahmood M. A comparative study on the effect of glazing and cooling for compound parabolic concentrator PV systems – Experimental and analytical investigations. Energy Convers Manage 2016;129:227–39. https://doi.org/10.1016/j.enconman.2016.10.028.

[42] Rahman M, Hasanuzzaman M, Rahim N. Effects of various parameters on PV-module power and efficiency. Energy Convers Manage 2015;103:348–58. https://doi.org/10.1016/j.enconman.2015.06.067.

[43] Aldihani A, Aldossary A, Mahmoud S, Al-Dadah R. The Effect of Cooling on the Performance of Photovoltaic Cells under Dusty Environmental Conditions. Energy Procedia 2014;61:2383–6. https://doi.org/10.1016/j.egypro.2014.12.010.

[44] Baïri A, Zarco-Pernia E, García de María J-M. A review on natural convection in enclosures for engineering applications. The particular case of the parallelogrammic diode cavity. Appl Therm Eng 2014;63(1):304–22. https://doi.org/10.1016/j.applthermaleng.2013.10.065.

[45] Tchinda R. Thermal behaviour of solar air heater with compound parabolic concentrator. Energy Convers Manage 2008;49(4):529–40. https://doi.org/10.1016/j.enconman.2007.08.004.

[46] Santos-González I, García-Valladares O, Ortega N, Gómez V. Numerical modeling and experimental analysis of the thermal performance of a Compound Parabolic Concentrator. Appl Therm Eng 2017;114:1152–60. https://doi.org/10.1016/j.applthermaleng.2016.10.100.

[47] Sharaf OZ, Orhan MF. Thermodynamic analysis and optimization of densely-packed receiver assembly components in high-concentration CPVT solar collectors. Energy Convers Manage 2016;121:113–44. https://doi.org/10.1016/j.enconman.2016.05.012.

[48] Chandan, Dey S, Iqbal SM, Reddy KS, Pesala B. Numerical modeling and performance assessment of elongated compound parabolic concentrator based LCPVT system. Renewable Energy 2021;167:199–216. https://doi.org/10.1016/j.renene.2020.11.076.

[49] Al-Nimr MDA, Dahdolan M-D-E. Modeling of a novel concentrated PV/T distillation system enhanced with a porous evaporator and an internal condenser. Sol Energy 2015;120:593–602. https://doi.org/10.1016/j.solener.2015.08.006.

[50] El-Samie MMA, Ju X, Zhang Z, Adam SA, Pan X, Xu C. Three-dimensional numerical investigation of a hybrid low concentrated photovoltaic/thermal system. Energy 2020;190:116436. https://doi.org/10.1016/j.energy.2019.116436.

[51] Li G, Lu Y, Xuan Q, Pei G, Ji J, Zhao X. Performance analysis on a crystalline silicon photovoltaic cell under non-uniform illumination distribution with a high electrical efficiency. Sol Energy 2020;203:275–83. https://doi.org/10.1016/j.solener.2020.04.060.

[52] Lamba R, Kaushik S. Modeling and performance analysis of a concentrated photovoltaic–thermoelectric hybrid power generation system. Energy Convers Manage 2016;115:288–98. https://doi.org/10.1016/j.enconman.2016.02.061.

[53] Soltani S, Kasaeian A, Sokhansefat T, Shafii MB. Performance investigation of a hybrid photovoltaic/thermoelectric system integrated with parabolic trough collector. Energy Convers Manage 2018;159:371–80. https://doi.org/10.1016/j.enconman.2017.12.091.

[54] Shadmehri M, Narei H, Ghasempour R, Shafii MB. Numerical simulation of a concentrating photovoltaic-thermal solar system combined with thermoelectric modules by coupling Finite Volume and Monte Carlo Ray-Tracing methods. Energy Convers Manage 2018;172:343–56. https://doi.org/10.1016/j.enconman.2018.07.034.

[55] Garg H, Adhikari R. Performance Analysis of a Combined Photovoltaic/Thermal (PV/T) Collector With Integrated CPC Troughs. ISES Solar World Congress 1999; 2000:349–53. https://doi.org/10.1016/b978-008043895-5/50226-5.

[56] Atheaya D, Tiwari A, Tiwari G, Al-Helal I. Performance evaluation of inverted absorber photovoltaic thermal compound parabolic concentrator (PVT-CPC): Constant flow rate mode. Appl Energy 2016;167:70–9. https://doi.org/10.1016/j.apenergy.2016.01.023.

[57] Saini V, Tripathi R, Tiwari G, Al-Helal I. Electrical and thermal energy assessment of series connected N partially covered photovoltaic thermal (PVT)-compound parabolic concentrator (CPC) collector for different solar cell materials. Appl Therm Eng 2018;128:1611–23. https://doi.org/10.1016/j.applthermaleng.2017.09.119.

[58] Chandan, Dey S, Suresh V, Iqbal M, Reddy KS, Pesala B. Thermal and Electrical Performance Assessment of Elongated Compound Parabolic Concentrator. Proceedings of the 7th International Conference on Advances in Energy Research Springer Proceedings in Energy 2020:633–43. doi:10.1007/978-981-15-5955-6_59.

[59] Reddy KS, Parthiban A, Mallick TK. Numerical modeling of heat losses in a line focusing solar compound parabolic concentrator with planar absorber. Appl Therm Eng 2020;181:115938. https://doi.org/10.1016/j.applthermaleng.2020.115938.

[60] Parthiban A, Reddy KS, Pesala B, Mallick TK. Effects of operational and environmental parameters on the performance of a solar photovoltaic-thermal collector. Energy Convers Manage 2020;205:112428. https://doi.org/10.1016/j.enconman.2019.112428.

[61] Evans DL. Simplified method for predicting photovoltaic array output. Sol Energy 1981;27(6):555–60. https://doi.org/10.1016/0038-092X(81)90051-7.

[62] Chandan, Suresh V, Iqbal SM, Reddy KS, Pesala B. 3-D numerical modelling and experimental investigation of coupled photovoltaic thermal and flat plate collector. Sol Energy 2021;224:195–209. https://doi.org/10.1016/j.solener.2021.05.079.

[63] McAdams WH. Heat Transmission. third ed. Tokyo, Japan: McGraw-Hill; 1954.

[64] Ali IMS, O'Donovan TS, Reddy K, Mallick TK. An optical analysis of a static 3-D solar concentrator. Sol Energy 2013;88:57–70. https://doi.org/10.1016/j.solener.2012.11.004.

[65] Duffie JA, Beckmann WA. Solar Energy. Thermal Processes. (Stichworte Teil 2). New York: Wiley & Sons; 1974.

[66] SolTrace. https://www.nrel.gov/csp/soltrace.html.

[67] Baig, H., Sellami, N., Bahaidarah, H., & Mallick, T. K. Optical analysis of a CPC based CPV/T system for application in the Kingdom of Saudi Arabia. 28th European Photovoltaic Solar Energy Conference and Exhibition; 2013.

[68] Tang F, Li G, Tang R. Design and optical performance of CPC based compound plane concentrators. Renewable Energy 2016;95:140–51. https://doi.org/10.1016/j.renene.2016.04.004.

[69] Wirz, M. Optical and thermal modeling of parabolic trough concentrator systems. (Doctoral dissertation, ETH Zurich 2014).

[70] Moghimi M, Craig K, Meyer J. A novel computational approach to combine the optical and thermal modelling of Linear Fresnel Collectors using the finite volume method. Sol Energy 2015;116:407–27. https://doi.org/10.1016/j.solener.2015.04.014.

[71] Salilih EM, Birhane YT. Modeling and Analysis of Photo-Voltaic Solar Panel under Constant Electric Load. Journal of Renewable Energy 2019;2019:1–10. https://doi.org/10.1155/2019/9639480.

[72] El Fouas C, Hajji B, Gagliano A, Tina GM, Aneli S. Numerical model and experimental validation of the electrical and thermal performances of photovoltaic/thermal plant. Energy Convers Manage 2020;220:112939. https://doi.org/10.1016/j.enconman.2020.112939.

[73] Ju X, Abd El-Samie MM, Xu C, Yu H, Pan X, Yang Y. A fully coupled numerical simulation of a hybrid concentrated photovoltaic/thermal system that employs a therminol VP-1 based nanofluid as a spectral beam filter. Appl Energy 2020;264:114701. https://doi.org/10.1016/j.apenergy.2020.114701.